Detection of T-cells and B-cells for Blood Analysis System Using Microfluidic Chip

Bilal TURAN

NAGOYA UNIVERSITY

GRADUATE SCHOOL OF ENGINEERING

Detection of T-cells and B-cells for Blood Analysis System Using Microfluidic Chip

A dissertation submitted for the degree of Doctor of Philosophy

Department of Micro-Nano Systems Engineering

Bilal TURAN

Acknowledgements

It is my great pleasure to acknowledge all the people who concern this work.

First, I would like to express my utmost gratitude to Professor Fumihito Arai, Department of Micro-Nano Systems Engineering, Nagoya University, Japan, for his constant support, guidance, encouragement, never ending patience and giving me a chance to be part of Arai Laboratory and showing me the path to becoming a leading researcher.

I would like to extend my sincere gratitude to Professor Yasuhisa Hasegawa from the Department of Micro-Nano Mechanical Science and Engineering, Professor Masahiro Ohka from the Graduate School of Informatics, Associate Professor Kousuke Sekiyama from the Department of Micro-Nano Mechanical Science and Engineering, Associate Professor Hisataka Maruyama from the Department of Micro-Nano Mechanical Science and Engineering for their kind agreement to being my doctoral committee members.

I would also like to personally thank Associate Professor Taisuke Masuda, Associate Professor Yoko Yamanishi, Associate Professor Akihiko Ichikawa, Associate Professor Lin Feng, Assistant Professor Rasit Asiloglu and Assistant Professor Shinya Sakuma for their constant support not only in my research but also in my personal life as well. And also Ms. Tsukamoto, and Ms. Ohsumi for alleviating the perils of life abroad. I would like to extend my thanks to all my colleagues for the colorful academic life they bestowed upon me.

Finally, I would like to express my deepest gratitude to my parents Mehmet Turan and Serife Turan for their endless patience, encouragement and support.

2019 *Bilal Turan*

Detection of T-cells and B-cells for Blood Analysis System Using Microfluidic Chip

Bilal Turan

Abstract

This thesis presents a blood analysis system for the isolation and detection of T-cells and B-cells. Providing an accurate count of total leukocytes from limited amounts of blood is a rather challenging ordeal.

First, we introduce the microfluidic chip that is designed and fabricated for the isolation of T-cells and B-cells. A micro-pillar array based gradual filtering with anti-clogging strategies such as escape routes is used to isolate the T-cells and B-cells from sub-microliter of whole blood. Based on the difference in size and deformability, leukocytes were separated from other blood cells by micropillar arrays. We confirmed the microfluidic chip is clog-free. Using the microfluidic chip, a trap rate of 99.8% is achieved.

Then we introduced a machine learning algorithm to detect T-cells and B-cells. The variability of cells in size, morphology and color intensity along with the emission spectrum crosstalk between fluorescence dyes make cell detection among pillars extremely difficult. A Support Vector Machine (SVM) supervised machine learning classifier based on both Histogram of Oriented Gradients (HOG) and color distribution features was proposed to distinguish T-cells and B-cells in a rapid and robust manner. HOG features were utilized to detect cells from background and noise; color distribution features were employed to alleviate the effect of fluorescence spectrum crosstalk. The experiment showed we achieved an average

detection accuracy of 94% for detecting T-cells and B-cells from the background. Furthermore, we also got 96% accuracy with cross validation to detect T-cells from B-cells.

Finally, we propose a Convolutional Neural Network (CNN) to further increase the accuracy of the detection. A CNN is trained and used to distinguish T-cells and B-cells with an accuracy rate of 98%, a specificity of 99% and a sensitivity of 97%. We also propose an HOG feature based SVM classifier to preselect the detection windows to accelerate the detection to process images in less than 10 mins. The proposed on-chip cell detecting and counting method will be useful for numerous applications in diagnosis and for monitoring diseases.

Contents

List of Figures

List of Tables

Chapter 1.

Introduction

1.1 Blood

Blood is vital to us. Unlike any other part of our anatomy, from the ancient times, its importance is acknowledged. Blood, or bleeding is what causes people to take the quickest action in caring for themselves. Losing 15-20 percent of the total blood volume, a man or woman will probably feel nausea, experience dizziness, have blurred vision, and is likely to faint [1]. Blood delivers oxygen and nutrients to the cells and cleanses the body by carrying the waste products. It consists of plasma and several types of cells. Figure 1.1 illustrates these blood

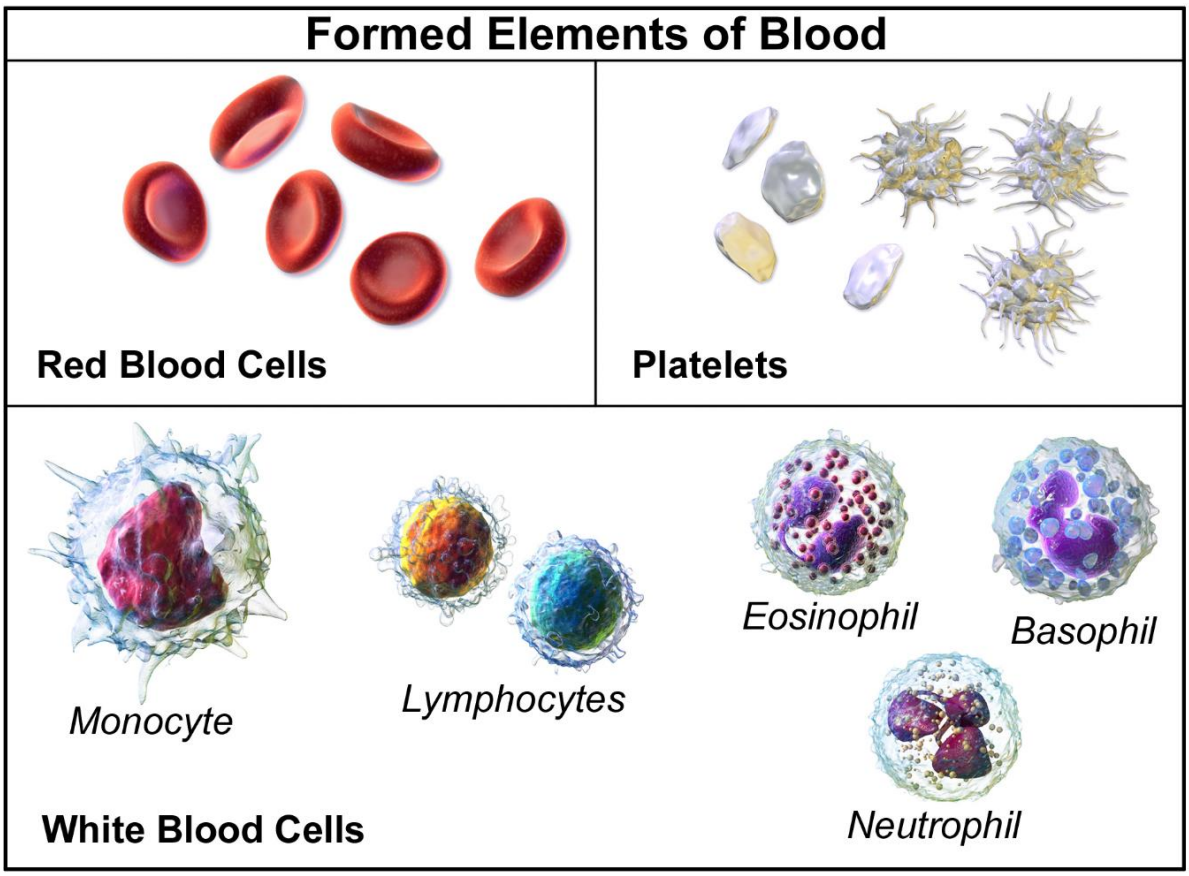

Figure 1.1 Blood cells [2].

cells which consist of red blood cells (RBCs), white blood cells (leukocytes), and platelets (thrombocytes).

1.1.1 Plasma

Blood plasma is the liquid part of the blood, that holds the blood cells in suspension. It can be separated from the blood by centrifuging whole blood until the blood cells settle at the bottom of the tube. Plasma comprises 55% of the blood volume and is mostly water. It contains dissolved proteins, glucose, clotting factors, hormones, carbon dioxide, oxygen and electrolytes [3]. The condition of blood plasma is an indication of health and diseases [4-6].

1.1.2 Red Blood Cells

Red blood cells contain the blood's hemoglobin, the iron-containing oxygen-transport protein which gives the red color to the cells and the blood. Red blood cells normally occupy 45% of the blood. Red blood does not have a nucleus or most organelles, giving more space for hemoglobin.

Blood diseases involving the red blood cells include anemia, hemolysis and polycythemias. Anemias characterized by low oxygen transport capacity of the blood, and could be caused by low red blood cell count [7], some abnormality of the red blood cells [8] or the hemoglobin [9-11]. Hemolysis is the term for the excessive breakdown of the red blood cells, which can be caused by the malaria parasite [12]. Polycythemias are diseases characterized by a surplus of red blood cells [13] which causes increased viscosity of the blood.

1.1.3 Platelets

Platelets react to bleeding from blood vessel injury by clumping and make a blood clot. Unless the injury is too big, they plug the hole. The blood clot is only a temporary solution, before the tissue is repaired. Platelets are disc shaped cytoplasm fragments from megakaryocytes and have no cell nucleus.

When platelet count is low [14], the bleeding might not stop, or there would be an increased tendency to bleed. Although too many platelets do not cause symptoms often, it might increase the risk of thrombus which is blood clotting inside blood vessels [15].

1.1.4 White Blood Cells

White blood cells are part of the immune system. They destroy and remove old cells as well as attack foreign invaders. Leukocytes are found throughout the body, including the blood and lymphatic system [16]. All white blood cells have nuclei, unlike red blood cells or platelets.

White blood cells are divided into five main types: neutrophils, eosinophils, basophils, monocytes and lymphocytes. These types can be distinguished by their physical and functional characteristics. Lymphocytes are further divided into T-cells, B-cells and NK cells.

White blood cells population count change dramatically in the presence of infections [17, 18], malignancies [19, 20], autoimmune disorders [21, 22], and chemical-induced hematotoxicity [23, 24]. Quantifying the number of leukocyte subpopulations, such as $CD3^+$ (T-cell), $CD19^+$ (B-cell), $CD4^+$ (helper T-cell), and $CD8^+$ (cytotoxic T-cell) cells, can be more informative of the immune response of the body comparing to the total leukocyte count. [25-30].

1.2 Blood Analysis Systems

Blood analysis are often used in health care to determine physiological and biochemical states. Biochemical tests such as basic metabolic panel analyzes the plasma and complete blood count provides a detailed count for cells in the blood. Blood count tests are one of the most requested blood tests in clinical laboratories. The idea of counting the cells in the blood was one of the earliest ways to study blood. This also marks the beginning of studying blood quantitatively. The credit for performing the first blood counts, goes to Professor Karl Vierordt. He used capillary tubes with a known diameter, so he could control the amount of blood that he was putting on top of a slide coated with albumen. After the blood dried, he placed a micrometer over the glass slide, and then he counted the blood cells. In his later works, he used a solution of gum Arabic to dilute the blood first. Although time consuming and tedious, his methods are considered to be fairly accurate [31]. Figure 1.2 illustrates example apparatuses that are used for cell counting in the early years of hematology. Most blood counts today include a complete blood

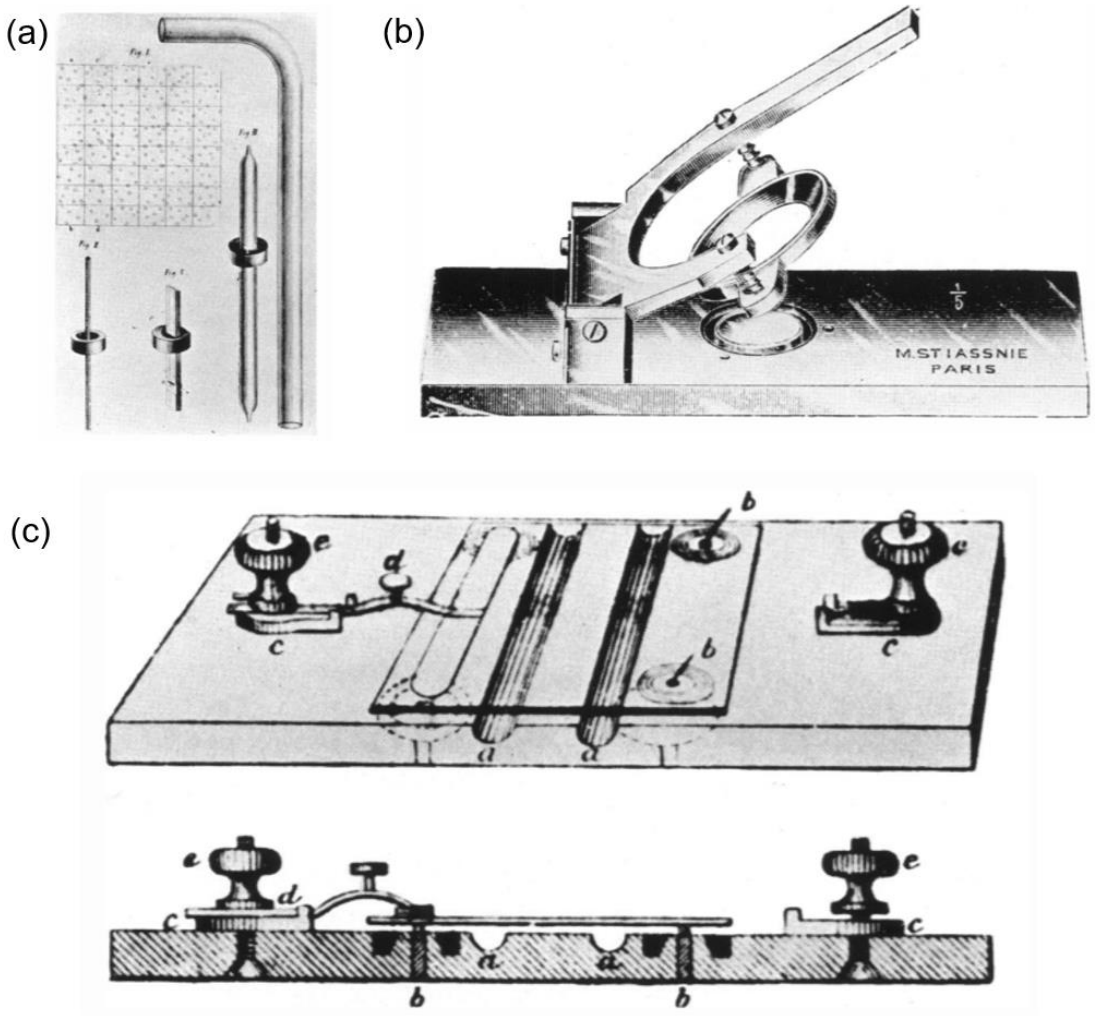

Figure 1.2 (a) Cramer's blood-counting apparatus, (b) Malassez's haemocytometer and (c) Alferow's haemocytometer [31].

count and leukocyte differential count that gives the percentage of each leukocyte type, such as neutrophils, eosinophils, basophils, monocytes, and lymphocytes [32].

1.2.1 Conventional Methods for Diagnostics

In 1954, Wallace Coulter developed an instrument that could measure cell size and count the absolute number of cells [33]. Over time, with the development of new instruments, cell

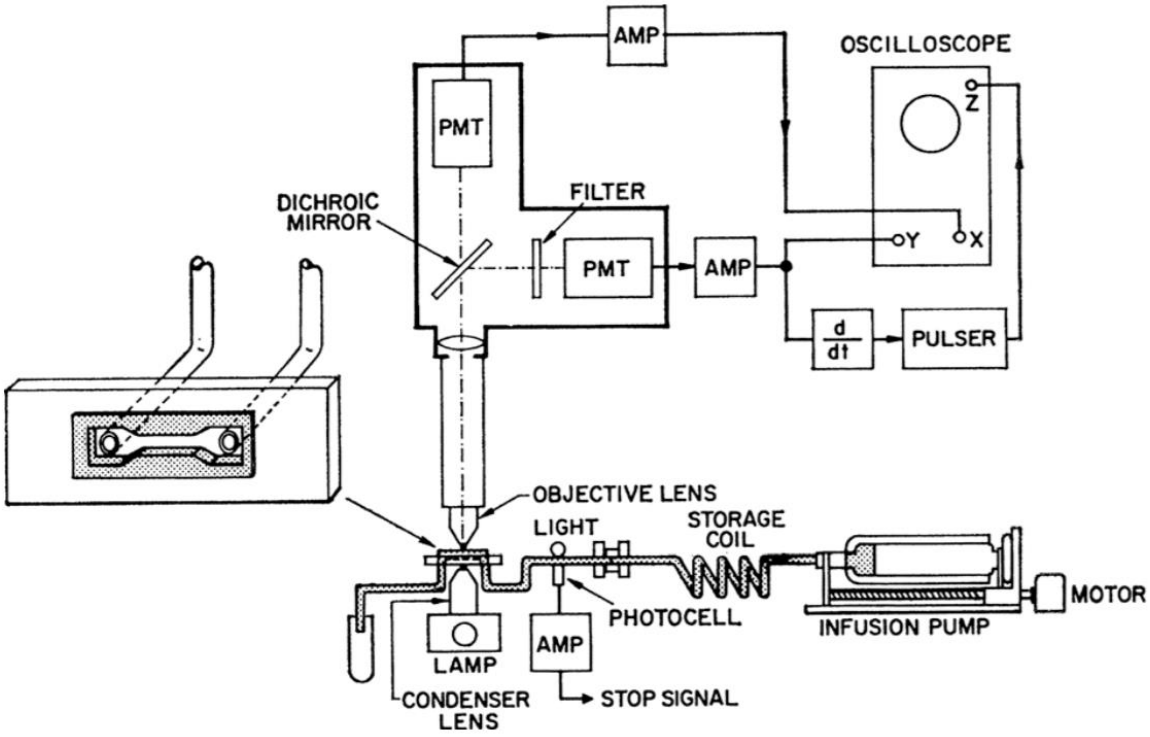

Figure 1.3 A schematic of a microfluidic flow cytometer constructed in 1965 by Kamentsky and used to analyze cells at 1000 cell s^{-1} [34].

size and nucleic acid content could be measured, by a two-dimensional approach that compared light scatter and light absorption [35, 36]. Figure 1.3 shows the instrument that was developed by Kamentsky in 1965. In the beginning these instruments were only used to investigate the functions of immune cells. Over time they started to be used in clinical facilities as diagnostics. Flow cytometry renders examination of cells possible. Cells are suspended in a stream of fluid, and hydrodynamically focused to flow one cell at a time through a microfluidic channel. A laser beam is focused at the flow of cells and scattered. Capturing the scattered light, size and granularity can be determined. Fluorescence dyes could be used to label the cells, which is excited when passing through the laser beam. The light emitted by fluorescence can be detected by fluorescence detectors. Figure 1.4 illustrates the flow cytometer and a sample output.

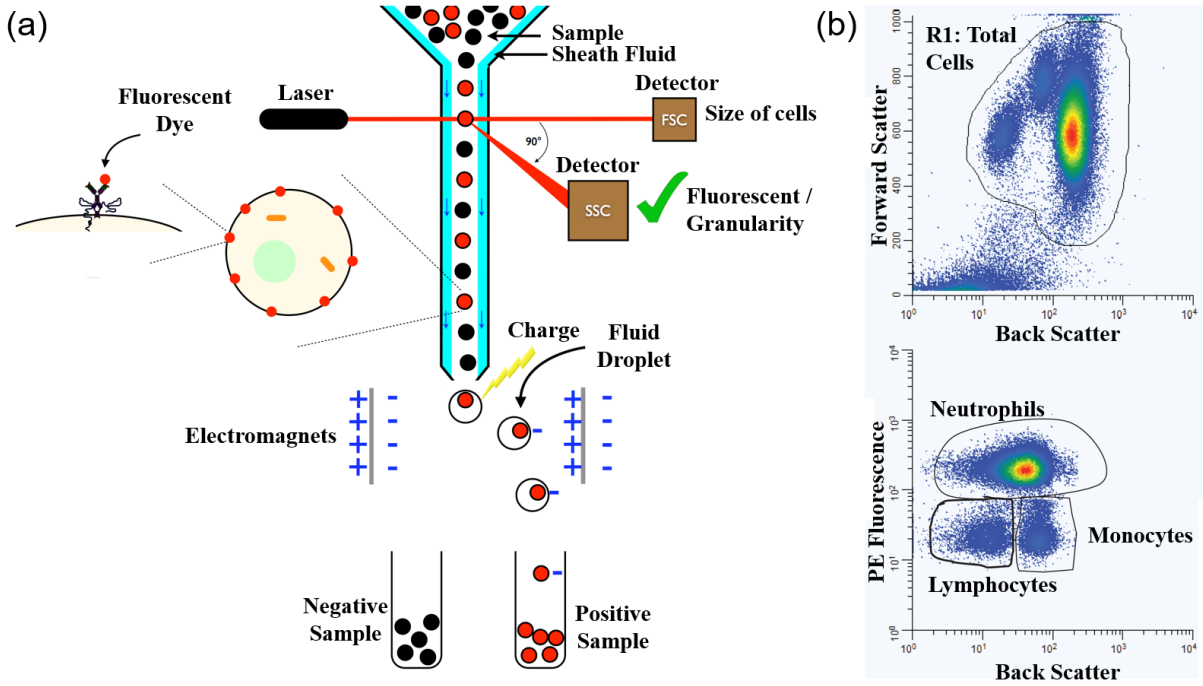

Figure 1.4 (a) Simplified notion of flow cytometry with sorting (b) sample output [37, 38].

After analyzing the cells, it is desirable to sort them into different channels or containers, to increase purity or to isolate rare cells. Recent flow cytometers can analyze and sort cells using multiple channels of fluorescence, several angles of scattered light, and other non-optical parameters such as impedance [34]. Currently, fluorescence-activated cells sorting (FACS) is used as the golden standard in biological research and clinical diagnostics to automatically determine the count for one or multiple types of cells [39, 40]. Figure 1.5 shows a modern flow cytometer.

FACS provides high throughput and high accuracy. However, requirements of large volume sample (in the order of mL) and expensive reagent, bulky equipment size, sophisticated costly optical component and the requirement of technical personnel make conventional FACS

Figure 1.5 Attune NxT Flow Cytometer, ThermoFisher Scientific [41]

prohibitive for point-of-care application. In addition, FACS is traditionally relied on for non-imaging technique by laser scattering and fluorescence emission for cell identification and hence there is no image information of cells [42]. Thus, it is crucial to develop a point-of-care blood analysis system, which is automated - or can be operated without any experts, requires a small amount of blood volume and can produce results in a matter of minutes [38]. Such a blood analysis system would have tremendous use in any clinical laboratory and especially in the developing world.

1.2.2 Blood Analysis Using Microfluidic Chips

In order to develop a compact blood analysis system, researchers are actively looking to microfluidic devices as the platform for the next generation translatable cell sorter. Microsystems enable cell-based assays, covering all the steps from cell culture, through selection and treatment, to biochemical analysis [43]. Microfluidic based devices are a proven technology for cellular handling as they can offer precise spatial and temporal control in a greatly miniaturized platform [34, 43]. Cell isolation can be grouped into categories by the

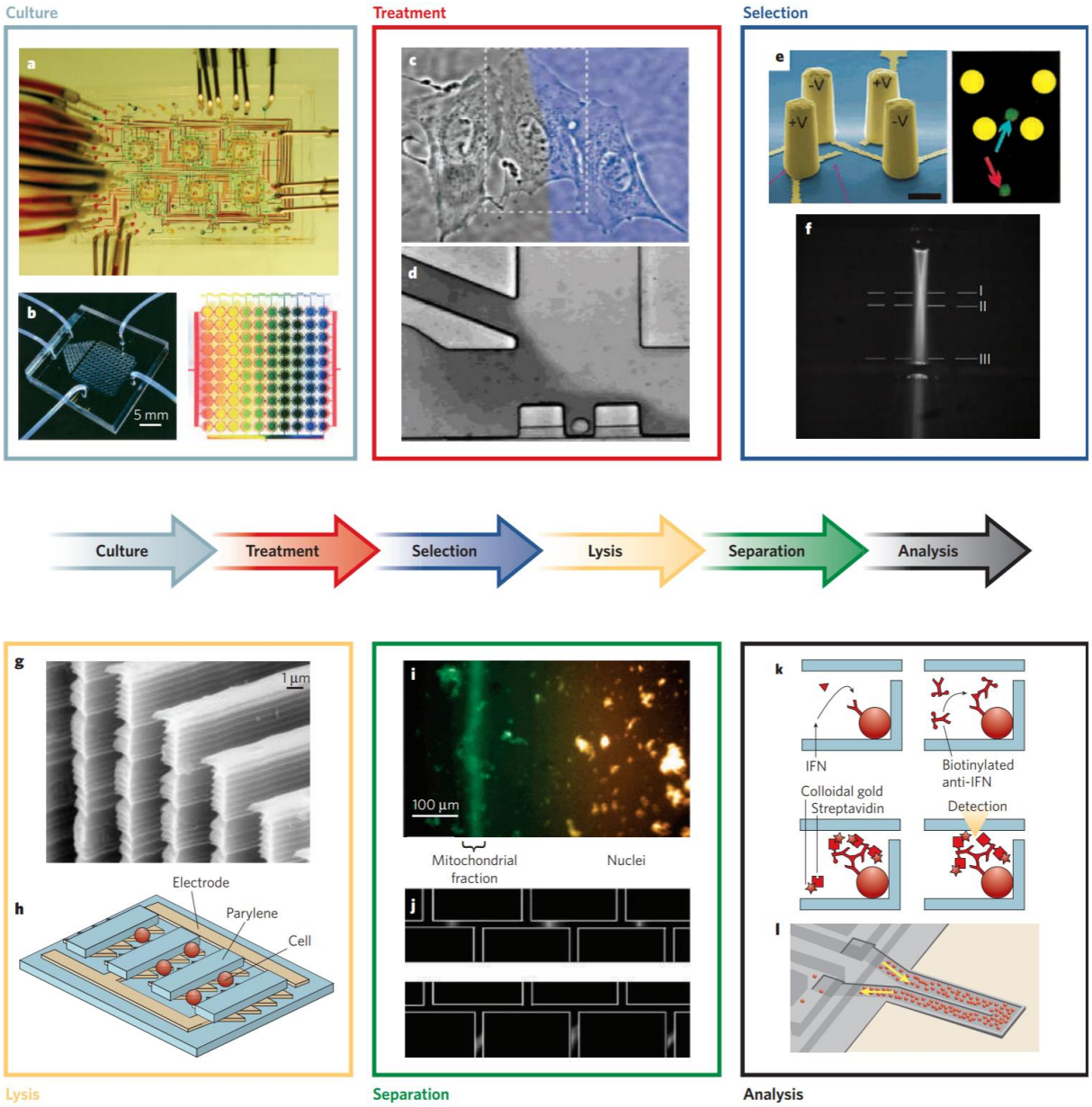

Figure 1.6 Microsystems enabling cell-based assays from cell culture to biochemical analysis. A collection of microsystems enabling cell-based assays, covering all the steps from cell culture, through selection and treatment, to biochemical analysis [43].

property of cells that are utilized, physical properties such as size, deformability, density and electrical charges; and biological properties such as marker proteins i.e. monoclonal antibody.

It is possible to combine different methods together, for the intended application. For cell isolation, there are several methods that utilize the physical characteristics of the cell [44]. It is possible to separate blood cells using non-inertial forces such as electrohydrodynamic [38], magnetic bead immunoassay [45], dielectric properties [46], optical force [47], magnetic [48], or acoustic [49, 50], as active separation techniques. These strategies might harm the cells or change their properties that render these unsuitable when the separated blood cells are intended to be used for another application. Microfluidic chips using these techniques are complex and suffer from low flow rates. On the other hand, passive separation techniques exploit the difference in size and deformability of cells in which they do not use any external force that might harm the cells, but isolate or trap the cells by the design of micropillars or pores inside the microfluidic chip [51]. These devices have simpler mechanical design and can support faster flow rates [52, 53].

1.2.2.1 Cell Isolation Based on Size and Deformability

The cells in the blood have various sizes and deformability. It is possible to exploit this difference for the isolation of blood cells. Leukocytes are larger than RBCs and platelets, using a microcavity array and designing its filtration conditions carefully it is possible to isolate leukocytes from the whole blood [52]. Figure 1.7 demonstrates the isolation system and isolation results. Leukocytes are trapped on the microcavity array while RBCs and platelets pass through.

The isolation of rare cells such as circulating tumor cells (CTCs) are crucial for the early diagnosis of cancer and rare cell research. An open-channel microfluidic chip for ease of recovery after isolation of CTCs is proposed [51]. Figure 1.8 shows the overview of the CTC isolation system. The air-liquid interface is utilized, so that blood cells drift towards the air-

liquid interface, and large cells such as CTCs are trapped by the micropillar arrays while smaller cells such as RBCs pass

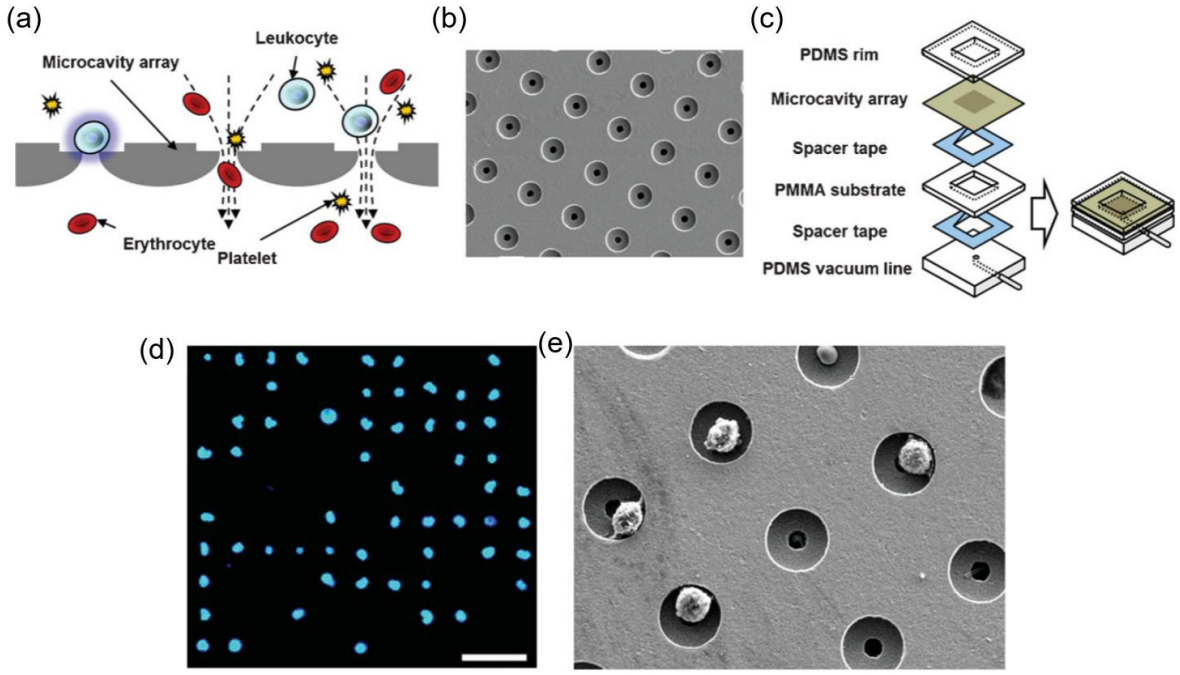

Figure 1.7 Microcavity array-based WBC counting device. (a) WBCs are trapped by microcavity array while RBCs pass through the gaps (b) Scanning electron microscope (SEM) image of microcavity array. (c) Schematic design of the device. (d) Fluorescent image of trapped RBCs. Scale bar; 50 μm. (e) SEM images of trapped RBCs [52].

through the gaps of the micropillar arrays. Air-liquid interface is maintained by the controlled introduction of the whole blood to the microfluidic chip by the help of motorized pumps. After the isolation of CTCs, using fluorescence microscopy the CTCs can be detected and recovered automatically using a motorized micropipette.

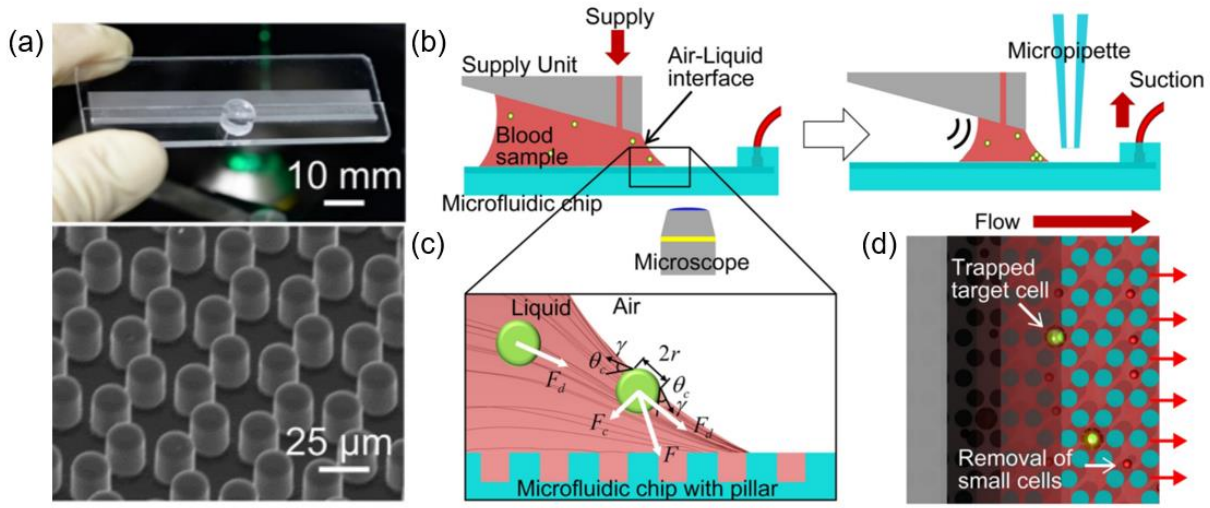

Figure 1.8 Overview of the CTC isolation system. (a) The image of the fabricated microfluidic chip and its SEM image. (b) Concept of the CTC isolation system. (c) CTCs move towards the meniscus of the air liquid interface and towards the bottom of the microfluidic chip by the forces acting on the CTSs. (d) Small cells such as RBCs pass through gaps between the micro-pillars, while larger cells such as CTCs and some of the WBCs get trapped [51].

1.2.2.2 Cell Isolation Based on Density

Density based microfluidic separation techniques can be used when separating particles which is not different in size but in their density. Cells encapsulated in mono-disperse polymer beads can be separated using standing surface acoustic waves (SSAWs), based on the density of the beads [49]. Figure 1.9 shows the separation of beads uniform in size but encapsulates different quantities of cells. The beads are first aligned at the center of microfluidic channel by hydrodynamic focusing. Then through acoustic radiation force, are separated by their density.

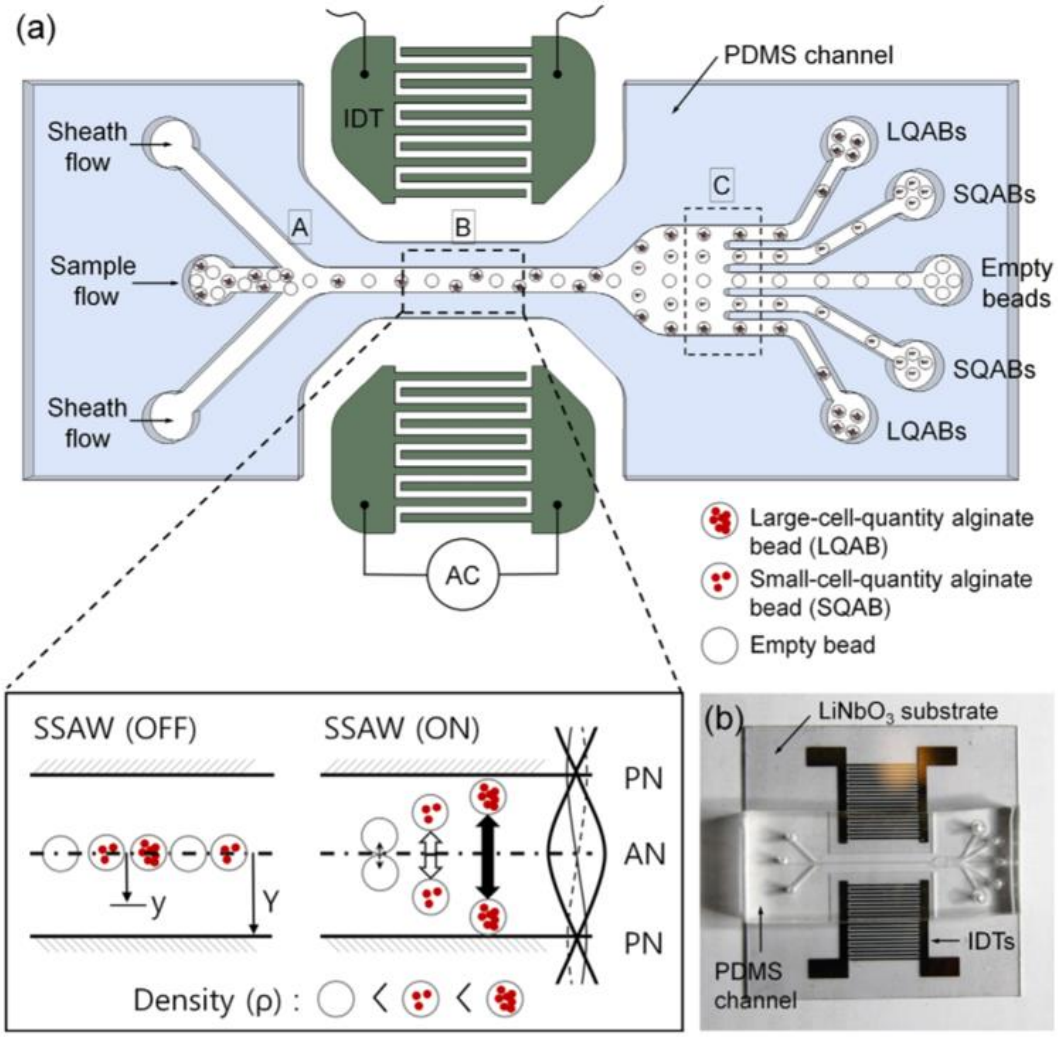

Figure 1.9 (a) Schematic illustration of the working principle of the standing surface acoustic waves (SSAWs). When acoustic radiation force is applied, beads are separated by their density. (b) The fabricated device [49].

1.2.2.3 Cell Detection Based on Electrical Analysis

Hematology analyzers which utilize the electrical properties study the blood cells according to their size and membrane properties. Cells are probed by using kHz and MHz frequencies with sensing electrodes [38]. Figure1.10 demonstrates the concept while Figure

1.11 illustrates the details of the microfluidic chip. It is possible to obtain the three-part WBC differential

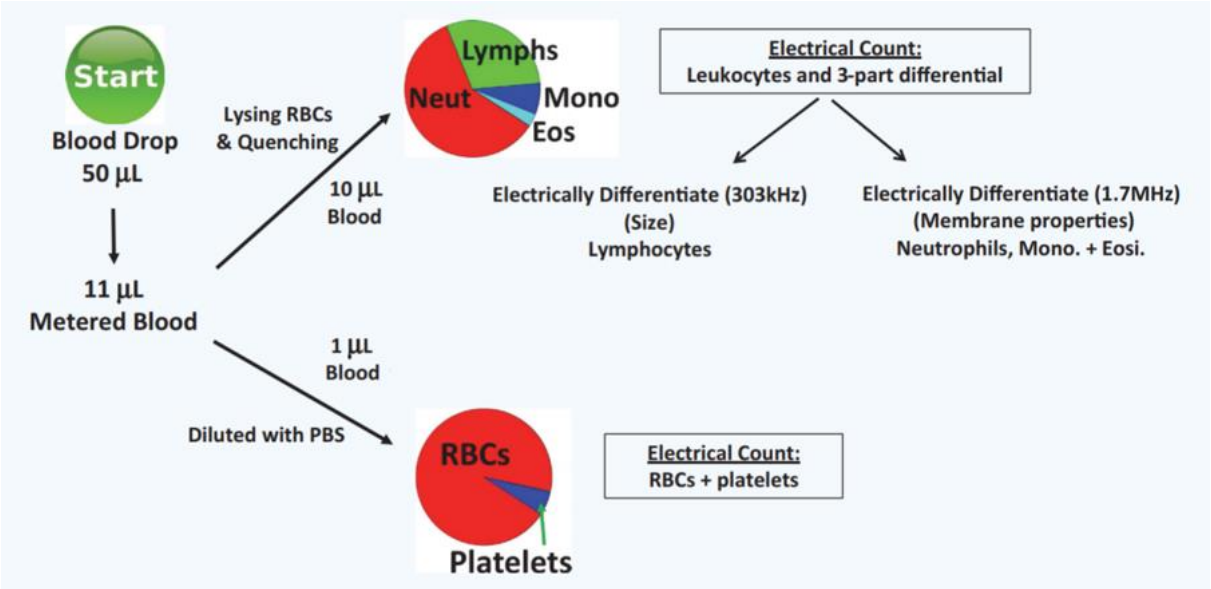

Figure 1.10 Illustration of the approach for blood cell counter. After lysing RBCs and quenching the lymphocytes, neutrophils, monocytes and eosinophils are counted. RBCs and platelets are counted after dilution on a separate chip [38].

and RBC/platelet counts, using only electrical analysis [38]. Lymphocytes can be separated from neutrophils, monocytes and eosinophils based on their different pulse amplitudes. Neutrophils can be differentiated from monocytes and eosinophils based on their membrane properties that is reflected by the impedance change at high frequencies which is greater than 1 MHz.

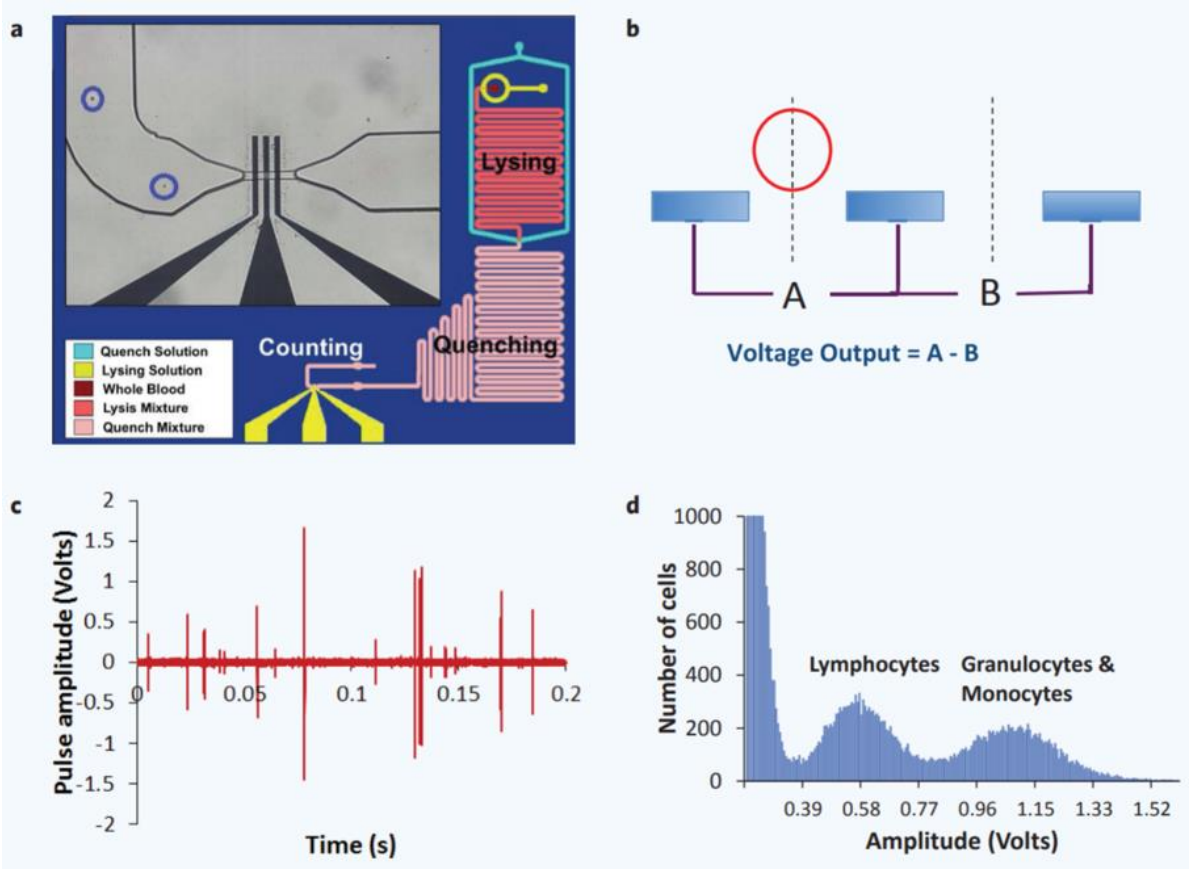

Figure 1.11 Overview of the leukocyte detection. (a) Schematic of the leukocyte counting chip with lysing, quenching and counter modules. (b) Schematic of the sensing region. (c) The typical voltage pulses obtained as the leukocytes pass through the counting region. (d) The amplitude histogram of the cell voltage pulses obtained with the sensing region [38].

1.2.2.4 Cell Isolation Based on Marker Proteins

Marker proteins are like fingerprints for cells. Using a specific antibody for a marker, it's possible to label and detect certain cells. The isolation of cells can be realized using magnetic beads coated with antibodies specific to the cell we want to separate [45]. After the mixing the cells with the magnetic beads, it is possible to isolate the target cells using a magnetic field and washing. Then purified cells are transported to the cell counting module, which excites the

fluorescence bound to the magnetic beads using a laser source, and the cells are counted using a photomultiplier tube. Figure 1.12 illustrates the device design and the steps of the isolation.

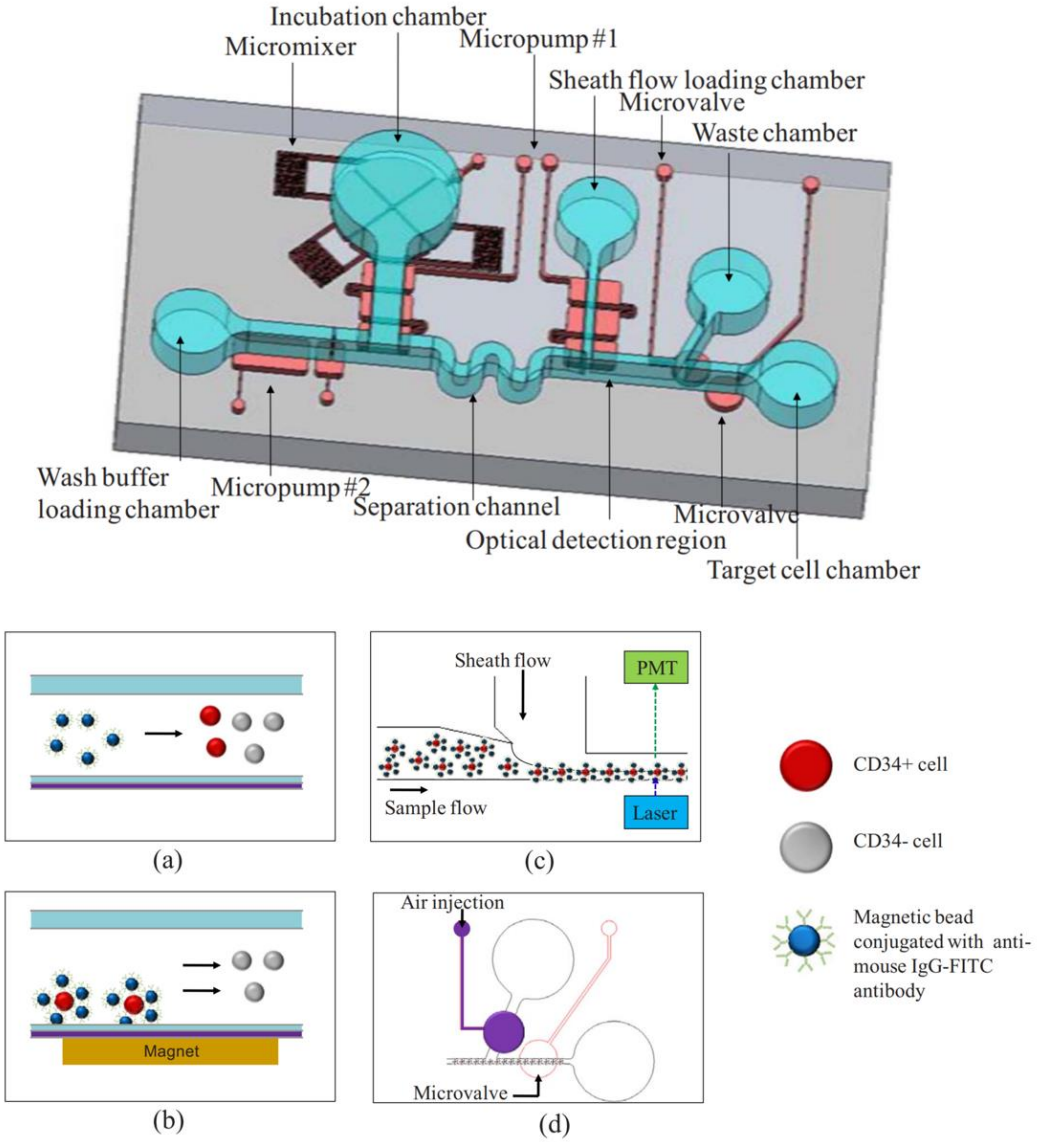

Figure 1.12 Cells are isolated by using magnetic beads. (a) Cells are mixed with magnetic beads, (b) then purified using washing in a magnetic field. (c-d) Fluorescence detection while cells pass through the optical detection region and sorting using microvalves [45].

1.3 Cell Imaging Technologies

Over the years with the development of new techniques and emerging technologies, cell analysis has evolved with regard to speed, sensitivity, spatial resolution, cost, etc. Every form of cell analysis represents a compromise. Three dimensional (3D) optical scanning microscopy can achieve great spatial resolution, but scanning takes time [54]. A standard optical microscopy has a variety of modes (transmitted light, scattered light, fluorescence, phase contrast, etc.), each of which provides distinct and complementary information about the cell [55] and is suitable to obtain a two-dimensional (2D) image of the cell. A flow cytometry measures fluorescence intensity and scattering from cells suspended in flow. Only a limited number of signals for each cell is available depending on the optical system, and spatial resolution is lost entirely, nevertheless it is possible to measure thousands of cells in a second [56].

The form of cell analysis and the method to process the data depends on the application and its time requirements. In case of real time detection and sorting of cells as in flow cytometry, only a fraction of a millisecond per cell is allowed. On the other hand, for confocal microscopy, 3D scans can be analyzed in detail offline. Due to the sheer amount of data from 3D scans or images, storing and processing raw cell data is not always possible and various features were extracted to simplify cell analysis [57]. Extracting simple features such as the size or circularity of a cell is significant in many cases, and the 2D image of the cell obtained via fluorescence optical microscopy will ease the processing and sharing of data. If the feature extracted from the 2D image is to be used for the detection and classification of cells, caution is required to prevent the loss of important information that might be included in an image. Hence, the extraction of features that contain most of the related information was researched and used for applications that require the detection and classification of cells [58]. With the improvement of

automation in image analysis and the ease of access to available algorithms, creating large datasets of cells and cell features became possible [59].

1.4 Machine Learning

Not so long-ago machine learning was only science fiction. Even before modern computers, the mind boggled with the idea of machines performing the tasks related to the mind. In the 18th century a chess playing automaton called “The Turk” fooled the masses into thinking that a simple clockwork machine can think and respond like a human would [60]. Although “The Turk” was a hoax and controlled by an operator, the questions raised by it about machines replacing humans in mental activities is salient. Two centuries after “The Turk”, in 1997 IBM’s Deep Blue won against world chess champion Garry Kasparov [61].

Alan Turing theorized how a machine would decipher and execute a set of instructions, which is considered the beginning of computer science [62]. Computers can progressively perform better on a specific task through algorithms and statistical models, which is called machine learning. Types of machine learning can be distinguished by the way they learn from the available data. In supervised learning, the data has known labels that are used to learn a model [63, 64]. When some part of the data is missing, and needs to be filled by the machine learning it is called semi-supervised learning [65, 66]. Algorithms like Support Vector Machines (SVM) is a type of supervised learning, which learns a boundary from the training data, and can classify the new data as one of the two classes using this boundary [67, 68]. When the labels of the data are not given, it is possible to make sense of the provided data which is called unsupervised learning [69, 70]. Neural networks such as autoencoders can learn features from data or remove noise in an unsupervised manner [71, 72]. As contrary to supervised and unsupervised learning, in reinforcement learning, there might not be pairs of inputs and labels,

and learning is possible through direct rewards to certain actions that learning algorithm takes. Google's DeepMind is an example of reinforced learning where a deep neural network learns how to play a computer game like a human would [73].

1.5 Thesis Overview

Our goal is the isolation of leukocytes from the whole blood without time consuming and cell damaging techniques such as centrifugation or RBC lysis. A pillar-based microfluidic chip and blood analysis system is proposed by our laboratory to isolate the leukocytes from the whole blood. The blood analysis system has support for automatic scanning of the filtration zone in the microfluidic chip. After the isolation, machine-learning methods for T-cells and B-cells detection is applied for robust and rapid detection.

T-cells and B-cells are dyed with immunofluorescence dyes and fluorescence images are used to detect T-cells and B-cells. A dataset consisting of more than 10,000 cell images labelled as T-cells and B-cells are generated as a result of this study and used to train the machine learning algorithms. Dataset is semi-automatically generated, and manually confirmed by an expert.

Figure 1.13 delineates the 5 chapters of this dissertation. We will first introduce the blood analysis system and talk about microfluidic chip design and isolation results in Chapter 2.

Chapter 3 focuses on Histogram of Oriented Gradients (HOGs) feature based Support Vector Machine (SVM) classification. We also discuss how the dataset is generated, and the tools that we supplied the experts to use for ease of identification. After the classifier is trained, using sliding window approach we have detected whether each detection window is a cell or not. Details of the training and detection will be discussed in further detail in the following sections.

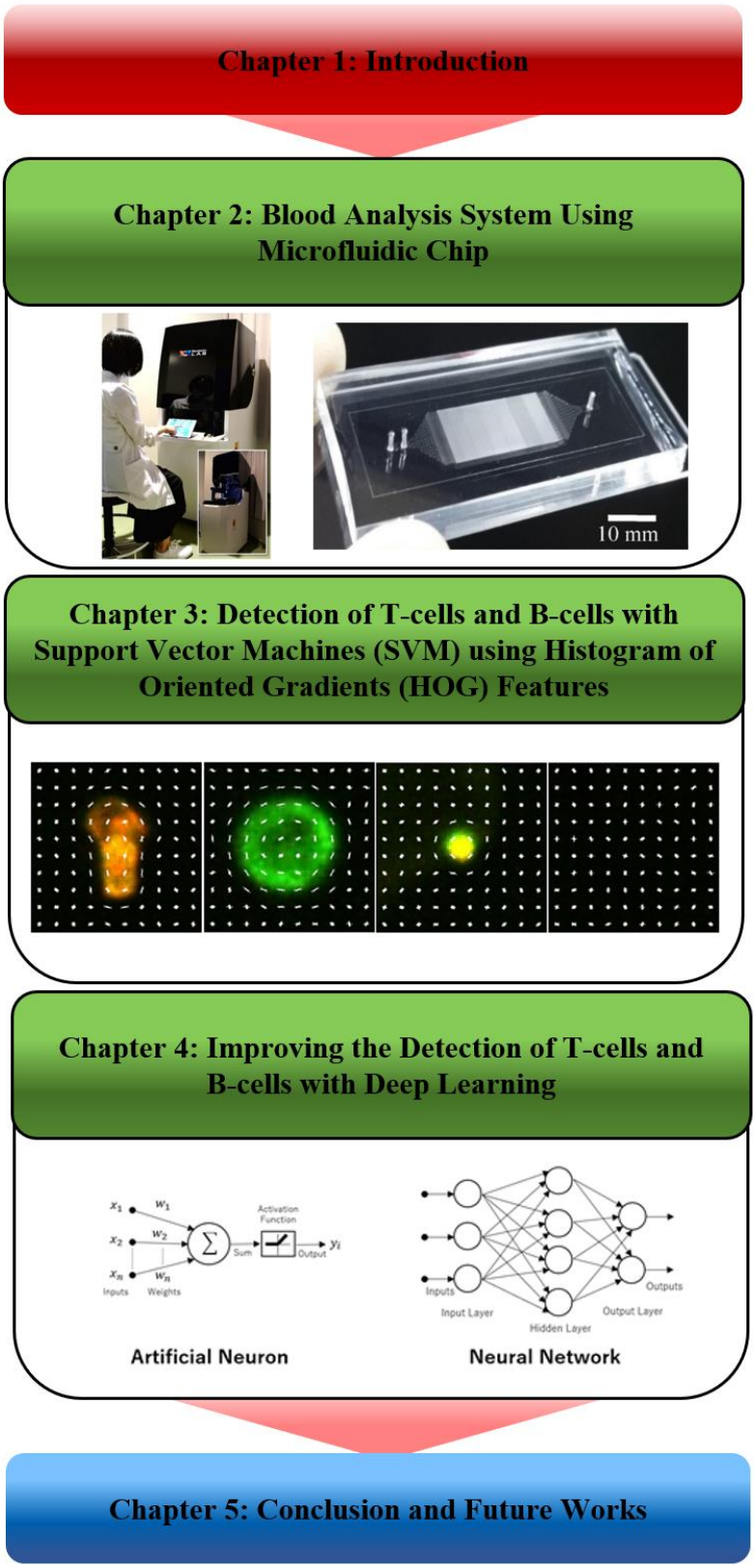

Figure 1.13 Outline of the dissertation.

Chapter 4 discusses the ways to improve the detection we have established in Chapter 3. A convolutional neural network (CNN) based approach is proposed. We have employed a pre-trained CNN and re-trained it ever slightly to detect T-cells and B-cells. We have discussed the time requirements of CNN and proposed a way to accelerate the detection by a two-layer classification. In the first layer, we use a HOG based classifier to preselect the detection windows, then CNN can be used to classify only the preselected windows to reduce amount of total detections that is required to achieve a similar detection accuracy.

In this study we propose to use a CNN to detect T-cells and B-cells from 2D fluorescence microscopy images. A pretrained convolutional neural network (CNN) is fine tuned to detect T-cells and B-cells from the background. A preselection method for detection windows using the HOG feature based SVM classifier is introduced to accelerate the detection process. Sliding window method is used on test images and each detection window in the image is classified by the trained CNN. The comparison of the performance between the trained CNN and our previous work which utilized the HOG feature based SVM classifier is demonstrated. Furthermore, the impact of the preselection method in performance is also discussed.

In the last chapter we will summarize our findings and discuss the future direction of our research.

Chapter 2.

Blood Analysis System Using Microfluidic Chip

2.1 Concept of Blood Analysis System

Our main goal is to develop a simple and highly efficient blood analysis system through the utilization of a microfluidic chip. The system must have a performance which is comparable to a standard flow cytometer used in clinical applications. Our system is to be able to identify the number of T-cells ($CD3^+$) and B-cells ($CD19^+$) among a cell population. For this purpose, our laboratory has developed a semi-automated cell separation system as Figure 2.1

demonstrates [51]. Apart from the microfluidic chip, the system includes a CMOS camera attached to a microscope for immunofluorescence imaging. XY motorized stages helps positioning the microfluidic chip and is used to take images of the whole chip in an automated way. The system is equipped with standard PC for image analysis. Upon capturing the target cell on the microfluidic chip, immunofluorescence imaging is used to identify the target cells. The whole chip is scanned automatically, and T-cells and B-cells are counted.

Figure 2.1 Rare cell sorter [51]

2.2 A Pillar-Based Microfluidic Chip

A pillar-based microfluidic chip is designed by our colleagues to isolate leukocytes from whole blood with high efficiency and without clogging [74]. All red blood cells and platelets must be removed during the processes of leukocyte counting and analysis, since they may disrupt the subsequent analysis of the leukocytes. In whole blood, red blood cells outnumber leukocytes approximately 1,000:1. The average size and number of each cell in human peripheral blood is shown in Table 1 [52]. As listed in Table 1 , the size difference of the blood cells makes pillar-based cell separation possible.

Table 1 Typical composition of peripheral blood [52]

Cell type	Number (/mL)	Size(mm)
Red Blood Cells	4,000,000–6,200,000	7.5–8.5
Platelets	150,000–400,000	2–3
Total leukocytes	4,500–11,000	
Neutrophils	1,800–7,700	15–17
Eosinophils	50–400	14
Basophils	25–1,000	10–14
Monocytes	100–800	15–20
Lymphocytes	1,000–4,000	6–15

The proposed microfluidic chip uses gradual size-based filtering which was developed for various cell applications [75-77]. However, problems such as low cell capture rate, low separation performance and high cell clogging remain. Hence, conducting a pre-treatment of sample is necessary such as hemolysis and centrifugation. A chip design that can overcome

these problems without the necessity of pre-treatment is proposed by our colleagues. Cells are captured in the gap between the pillars and excess cells are introduced to the escape routes in the micro-pillar array, thus preventing clogging. This in turn reduces the time required for the diagnosis by eliminating sample pre-treatment.

2.2.1 Chip Design

Figure 2.2 (a-b) demonstrates the concept of the microfluidic chip. Since there is not much work done on how to design such a microfluidic chip in the literature, the proposed microfluidic chip is designed through a trial and error process based on the size and deformability of the cells [74]. The microfluidic chip employs gradual size-based filtration with gap sizes ranging from 3 to 15 μm. Micro-pillar arrays with bigger gap sizes are intended for larger cells such as leukocytes whose size can differ between 7 to 30 μm as listed in Table 1. If the gap is too large, cells might escape due to their deformability, resulting in losses in such devices [78-80]. A non-pillar area that is termed as an escape route, whose width is greater than the gap between micro-pillars, is used in the pillar-based cell filtration area to decrease pressure during trapping.

The fluid pressure increases from bigger gap sizes to smaller gap sizes such as 3 μm and 4 μm. The escaped cells will flow through the least resistance path which is the empty pillar gap in the next row. The escape route is the preferred path in case micro-pillar gaps are occupied by cells. Red blood cells are more flexible and can hence suffer deformability up to 2 μm and can escape through all the micro-pillar arrays [81]. Hence, the direct separation of leukocytes from whole blood is possible.

The height of the microfluidic chip is also important for the accuracy of the detection of the leukocytes after trapping. As Figure 2.2 (c-d) shows if the microfluidic chip is too high then more than one leukocyte might be trapped in the same gap and this might cause errors during

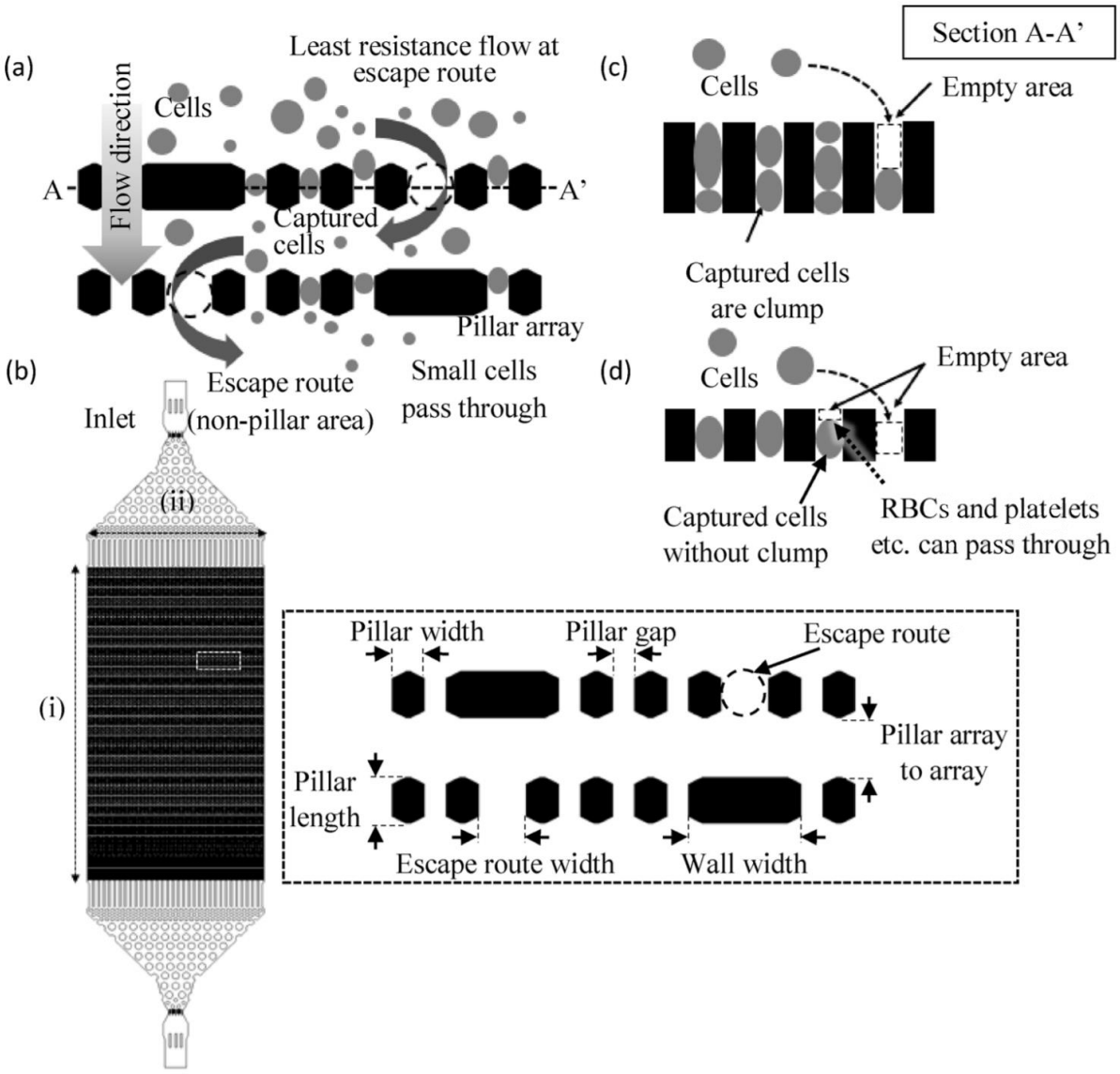

Figure 2.2 The concept for preventing clogging of cells. (a) When WBCs are captured in the gaps between the pillars, and other cells will keep flowing through the escape routes which is the path of least resistance. (b) Design of the microfluidic chip (c-d) Side view of the pillars. Cells overlap if the micro-pillar is high (i.e., 20 μm or more) [74].

detection of the leukocytes from fluorescence images. The height of the microchannel is designed to be 13 μm via trial and error. The total capture area is 10 mm in width and 20 mm in length.

Table 2 provides the details of the microfluidic chip design. Most of the micro-pillars have a size of 20 μm x 14 μm. It is important for micro-pillars to have a size big enough to endure the demolding process during fabrication. If the strength of the pillars is not enough, they might easily break. As Table 2 shows, the size of the escape route is related to the gap size. With a larger escape route, more cells can pass through. Small target cells are anticipated to be captured at smaller pillar gaps.

Table 2 Details of the microfluidic chip design [74].

Pillar gap (μm)	Pillar length (μm)	Pillar width (μm)	Wall width (μm)	Number of arrays	Pillar array row-to-row (μm)	Number of pillar gaps	Escape route width (μm)	Escape route number per pillar arrays
15	20	14	-	12	25	4140	-	-
14	20	14	200	12	25	5,850	30	13
13	20	14	200	12	25	2,652	30	13
12	20	14	200	12	25	2,652	30	13
11	20	14	200	12	25	2,652	30	13
10	20	14	200	12	25	7,800	25	13
9	20	14	48	48	25	14,112	20	49
8	20	14	48	60	25	18,000	20	50
6	20	14	58	60	25	19,080	20	53
5	20	14	44	60	25	20,520	15	57
4	22	20	54	48	25	13,536	14	47
3	22	20	42	40	15	14,520	6	33

2.2.2 Microfluidic Chip Fabrication

The process of the microfluidic chip fabrication is based on the soft-lithography technique. A master mold is made using a Si-wafer. Via the employment of a molding process the microchannel part is made of poly-dimethylsiloxane (PDMS). Following this, the microchannel part is bonded with a glass plate in order to create the microfluidic chip. Firstly, the photomask was prepared using laser lithography (DWL66FS, Heidelberg Instruments Mikrotechnik GmbH, Heidelberg, Germany). The Si-wafer (thickness 500 μm, Matsuzaki Ltd., Japan) is then spin coated using an epoxy-based photoresist (SU-8 3010, Microchem, MA, USA) to the required thickness (~10 μm). The photoresist is cured with a soft bake (95 °C, 30 min) process. After this, the Si-wafer was exposed to UV light with the photomask using a mask aligner (Suss MA6, SUSS MicroTec, Germany). Then the Si-wafer was developed and dry-etched utilizing a deep reactive ion etching process (RIE-800, Samco, Japan). Plasma polymerization (RIE-800, Samco, Japan) of octafluorocyclobutane (C_4F_8) was used for passivation of the Si-mold to ensure that the surface is non-adhesive during repeated PDMS microfluidic chip demolding processes. PDMS microchannel part was prepared with a PDMS pre-polymer (Silpot 184, Dow Corning Toray Co., Ltd., Japan) mixed with a curing agent in a 10:1 (w/w) ratio, and then it was poured onto the Si-mold and baked for 45 minutes at 85°C. The cured PDMS was then demolded and the PDMS microchannel part was treated with an O_2 plasma (Femto Science Cute-MPR, South Korea) to finish the PDMS-glass bonding process. Figure 2.3 shows the process steps for microchannel fabrication [74]. Figure 2.4 shows the fabricated PDMS microfluidic chip.

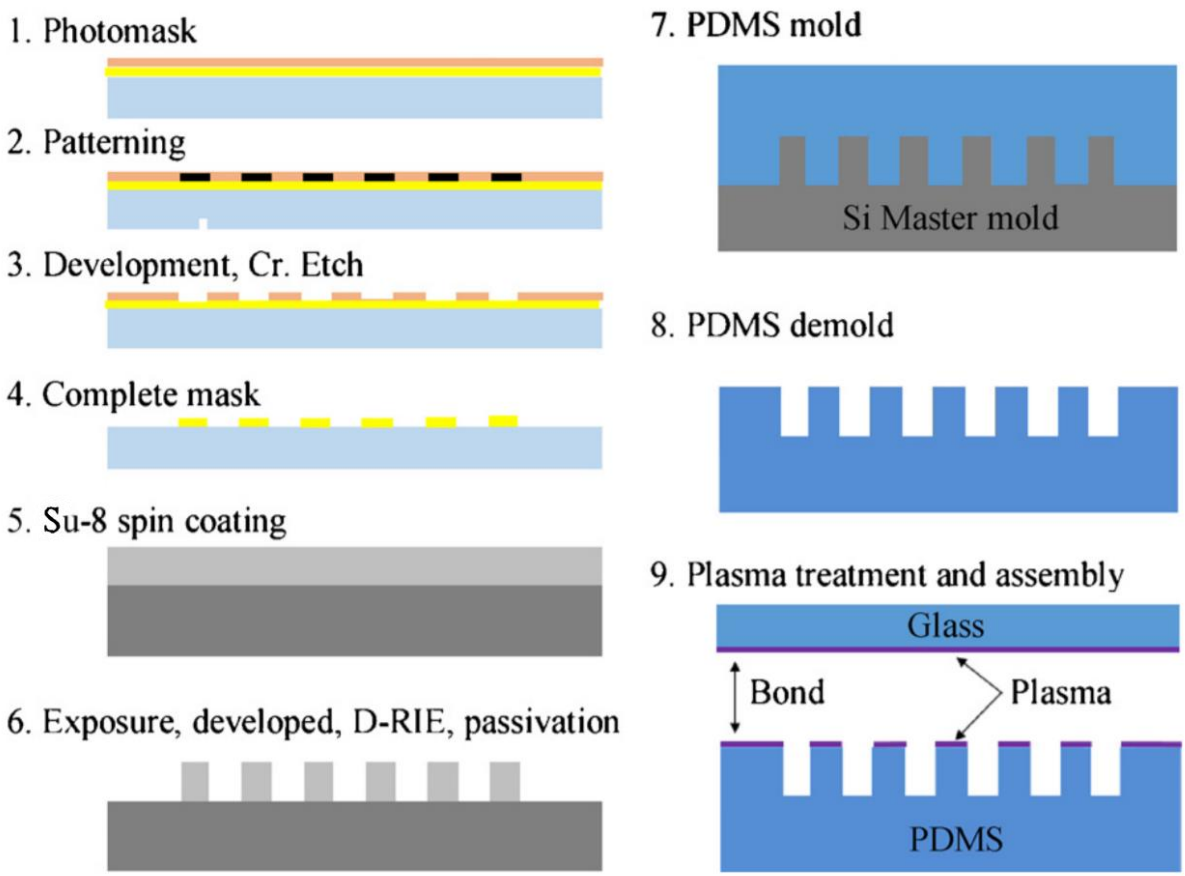

Figure 2.3 Fabrication process of the microfluidic chip [74].

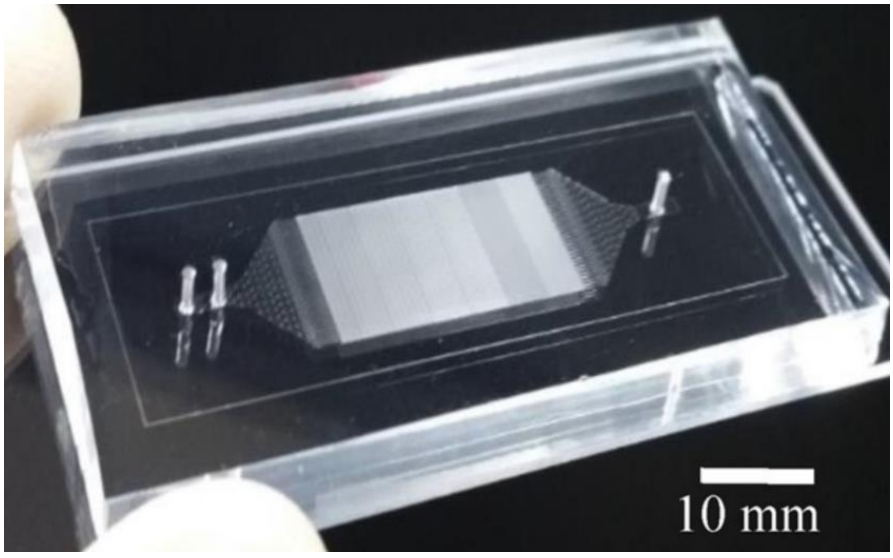

Figure 2.4 Fabricated PDMS microfluidic chip [74].

2.2.3 Sample Preparation

Human blood samples were collected from healthy donors at the National Hospital Organization Nagoya Medical Center. The study protocol was reviewed and approved by the institutional review board, and written informed consent was obtained from all participants. In order to prevent coagulation, the samples were collected in a collection tube with EDTA and were used within 24 hours. For T-cells and B-cells detection, the blood sample was mixed with a two-color direct immunofluorescence reagent (BD Simultest^{TM} CD3-FITC(Ex 494 nm, Em 520 nm) / CD19-PE(Ex 496 nm, Em 578 nm), BD Bioscience, San Jose, CA) and incubated at room temperature for 15 minutes. Then the prepared sample was diluted 10 times using the dilution buffer (PBS + EDTA) and kept in the dark at room temperature until the experiments were conducted.

2.2.4 Cell Isolation Results

$CD3^+$ and $CD19^+$ cells are successfully captured using the microfluidic chip. The cell isolation experiment is performed for several times, and the results are compared with a flow cytometer (BD FACSCanto^{TM} II, BD Biosciences, San Jose, CA, USA) as a reference instrument. When introducing the sample to the microfluidic chip, sample flow speed is the deciding factor on the capture rate of the leukocytes and where they are captured, since the deformability of cells highly depends on fluid stress [82]. Sample flow speed is decided as 3 μL/min empirically, where many cells can be captured and faster sample introduction becomes possible [74]. First, sheath liquid is introduced (PBS with 5 mM EDTA) into the microfluidic chip to remove the bubbles. Then 1 μL whole blood (Total sample volume: 10 μL) is introduced into the chip and collected out of the chip in a tube. Following the sample introduction, the fluorescence of T-cells and B-cells were excited (488 nm) and the filtration zone on the chip

was scanned automatically. As Figure 2.4 illustrates, most T-cells (green) and B-cells (yellow) were captured in 5 µm to 8 µm gaps area.

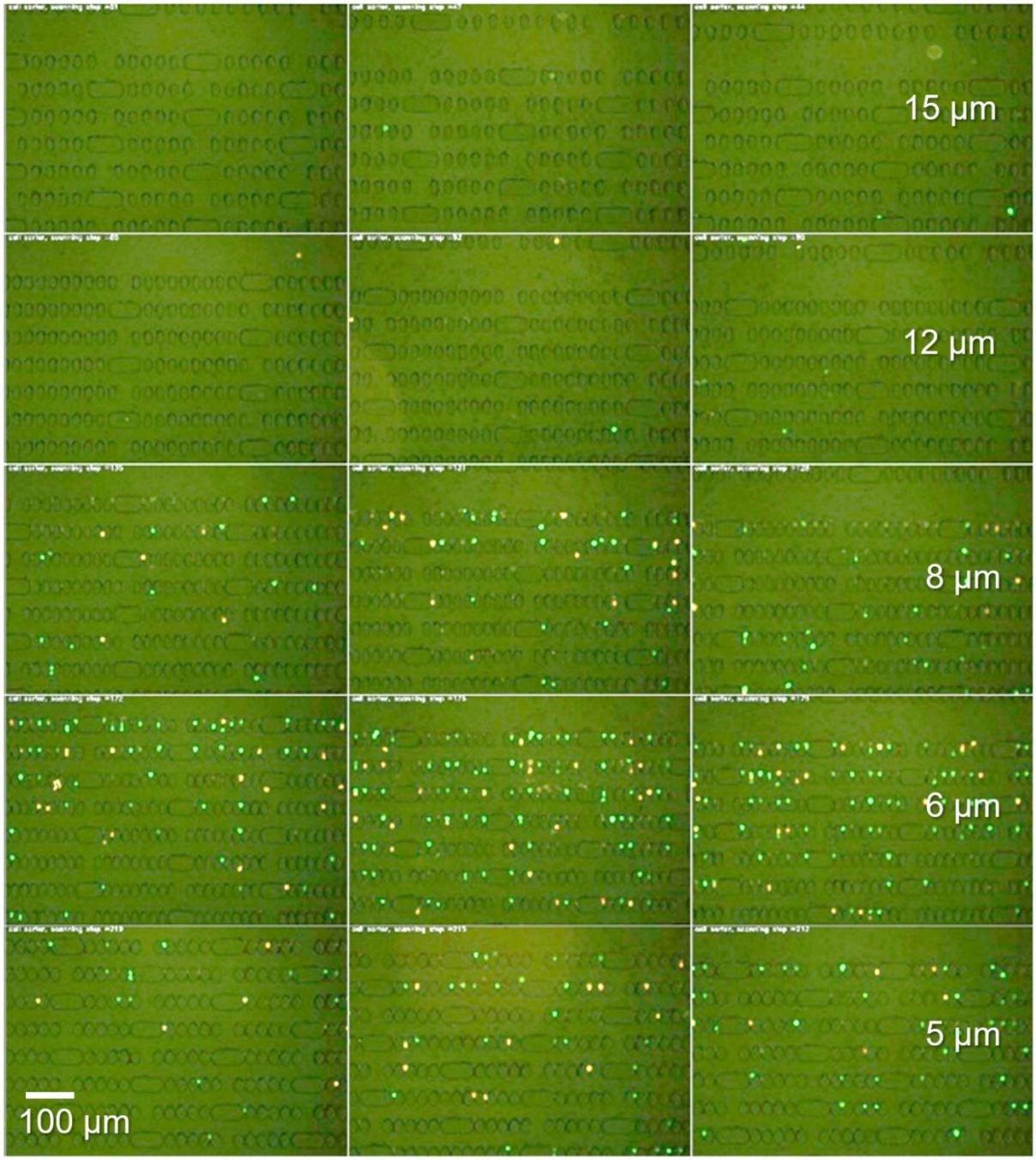

Figure 2.5 Partial scanned images of the filtration zone for T and B lymphocytes.

Through several experiments our colleagues confirmed that the cell capture area of the microfluidic chip remains clog-free. By counting the leukocytes that did not get trapped by the microfluidic chip and ended up flowing to the outlet we have confirmed a trap rate of 99.8% in capturing leukocytes using the microfluidic chip, and through the comparison with a flow cytometer the ratio of $CD3^+$ and $CD19^+$ found to have a coefficient of r = 0.9876 and a coefficient of variation (CV) of 2.77% which proves that our system and microfluidic chip can be successfully used to isolate leukocytes from whole blood [74].

2.3 System Configuration

Figure 2.6 shows the system configuration used in our experiments. The single inlet single outlet fabricated device was connected to a gastight syringe pump (1710 TLLX SYR, Hamilton, USA). The syringe pump and XY scanning stage were manipulated by a high precision controller (QT-AMH2, Chuo Precision Industrial, Japan), through serial communication via PC Controller.

The imaging system is designed to be able to detect weak fluorescence signals from a cell. A 488 nm light source (Lumencor Inc., Beaverton, OR, USA) is used to excite fluorescence CD3-FITC(Ex 494 nm, Em 520 nm) and CD19-PE(Ex 496 nm, Em 578 nm). For multicolor fluorescence detection a dichroic mirror (DM505, Olympus, Japan) is utilized. An emission band-pass filter for the wavelength range of 500-650 nm (Semrock, Rochester, NY, USA) is used, to improve the signal to noise ratio for the emission light. A wide range filter is utilized to cover the entire FITC and PE fluorescence emission spectrum, since cell detection is compromised when the detection filter spectrum is limited [74].

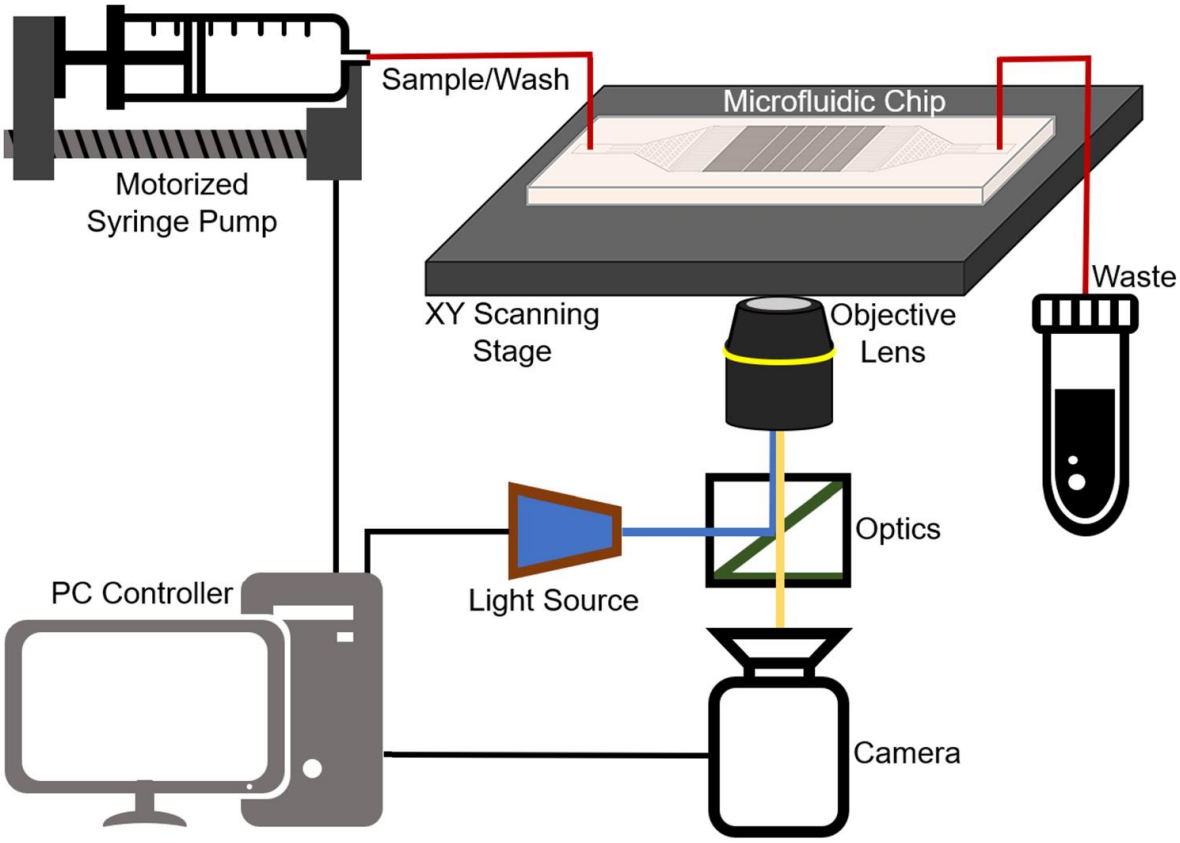

Figure 2.6 System configuration.

The relative intensity of fluorescence light emission depends on the expression of cell surface antigen [83] and the type of fluorochrome [84]. Fluorescence emission signals are weak, so to alleviate this a high sensitivity CMOS-camera (ASI178 MC, Zhen Wang Optical Company, China, 3,096 x 2,080, pixel size 2.4 μm) is installed on the eyepiece body tube of the microscope. Utilizing the high sensitivity camera, low noise images could be acquired. The filtration zone of the microfluidic chip was scanned frame by frame, and after an image was acquired the chip was moved using motorized stages. The total area of the filtration zone can be covered by 420 images and the scanning time is 14 mins.

Automation of the blood analysis system is important for the ease of use such as controlling the XY stages and sample flow speeds through a user-friendly interface. After the chip is placed

on the XY stage and the connections are made, the rest of the isolation and detection is semi-automated. The simple user interface enables inexperienced users to easily change the flow speed, positioning of the microfluidic chip and controlling of the light sources. Although the initial positioning of the microfluidic chip has to be manually set by moving the XY stages through the user interface and few parameters needs to be set, image acquisition is automated. Thus, user do not have to worry about accurately scanning the filtration zone, or scanning the same spot twice. After the acquisition of images, detection and counting of T-cells and B-cells is possible.

Chapter 3.

Detection of T-cells and B-cells with Support Vector Machines (SVM) using Histogram of Oriented Gradients (HOG) Features

3.1 Introduction

After isolation, captured cells are usually distinguished from the microfluidic chip's fluorescent microscopy images. Using different cell markers, we can detect, identify and count cells. However, cells imaged by fluorescence microscopy exhibit heterogeneous intensity levels and are often badly contrasted. The variability of cell size and morphology, differences in

illumination over time and across the whole microfluidic chip hamper the ability to specify a global set of parameters for cell detection algorithms over the whole experiment. Furthermore, there are serious spectrum crosstalk between fluorescence dyes when performing dual or multiple cells detection. The available algorithms for illumination correction and segmentation do not perform well enough to achieve satisfying results on many experiments [85].

Therefore, there is a strong motivation for the development of an automatic cell detection and counting method [86]. A machine learning algorithm, with an appropriate feature extractor for the application is the key to success. For this, Histogram of Oriented Gradients (HOG) represents a robust feature descriptor used in computer vision area for object detection [87]. One of the key advantages of HOG is being able to describe object orientation while showing invariance to geometric and photometric transformations because it operates in localized regions. In other words, HOG tends to be unaffected by changes in shapes and lighting, which appear in larger spatial regions. These advantages make HOG features fit our situation especially well due to the cell's variability in intensity and shape on pillar based microfluidic chip. A support vector machine (SVM) can be used to classify HOG features. SVM is a supervised machine learning algorithm, which creates a model according to the training data, and then the test data can be classified according to the said model [88].

The framework of object detection with Histogram of Oriented Gradients (HOG) and color features is illustrated by the block diagram in Figure 3.1. It consists of separate training and testing phases. In the training phase, we trained two separate SVMs to detect cells from background and to identify the detected cells as T-cells or B-cells. First using the dataset that is generated from the dual dyed images, a linear-kernel SVM is trained to detect cells from background. Then, the images that are dyed with only singe dye are exhaustively searched using the sliding window method, finding HOG for each window and classified by the first SVM.

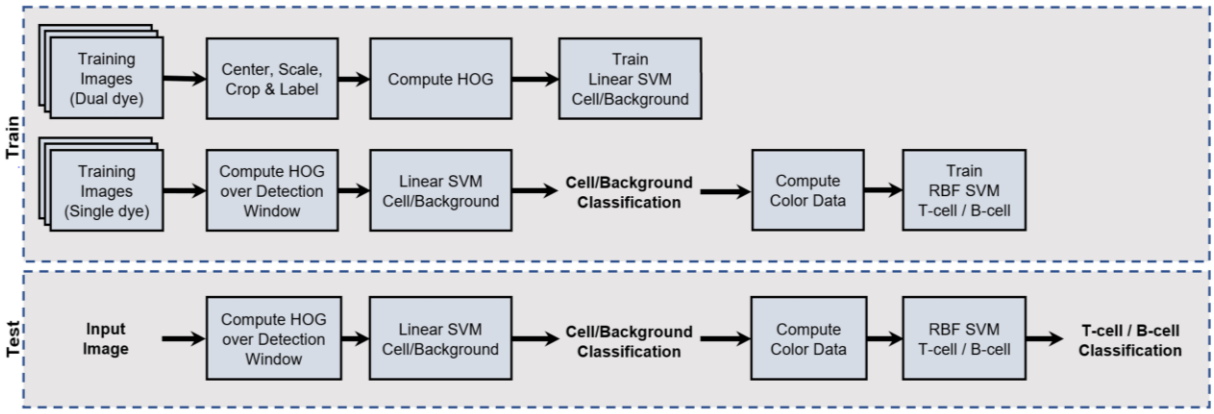

Figure 3.1 The steps for T-cell and B-cell detection using machine learning. HOG and color features are learned from training images and using SVM cells are detected from test images.

Found cells are then used for their color information to train a Radial Basis Function (RBF)-kernel SVM [88] to identify T-cells from B-cells. Although RBF-SVM is timewise costly, it gives better accuracy. In the testing phase, unseen images are scanned with sliding window and HOG features are generated from the position of each window in the image. These features are classified as cell or background with the linear SVM classifier, then classified cells are further processed to get the color information and classified as T-cells or B-cells using the RBF SVM.

3.2 Dataset

There is no standard dataset for fluorescent cell images, so we created a custom dataset to be used in our detection algorithms. To train and test the detection of cells we used the scan images from 10 experiments that are dyed with the dual dye. Seven experiments are used as training data which consist of 2,940 images. Another three experiments consisting of 1,320 images are reserved for the test. A total of 6,200 cell images and 35,000 background images are gathered semi-automatically from the training images. Figure 3.2 shows a sample from this dataset.

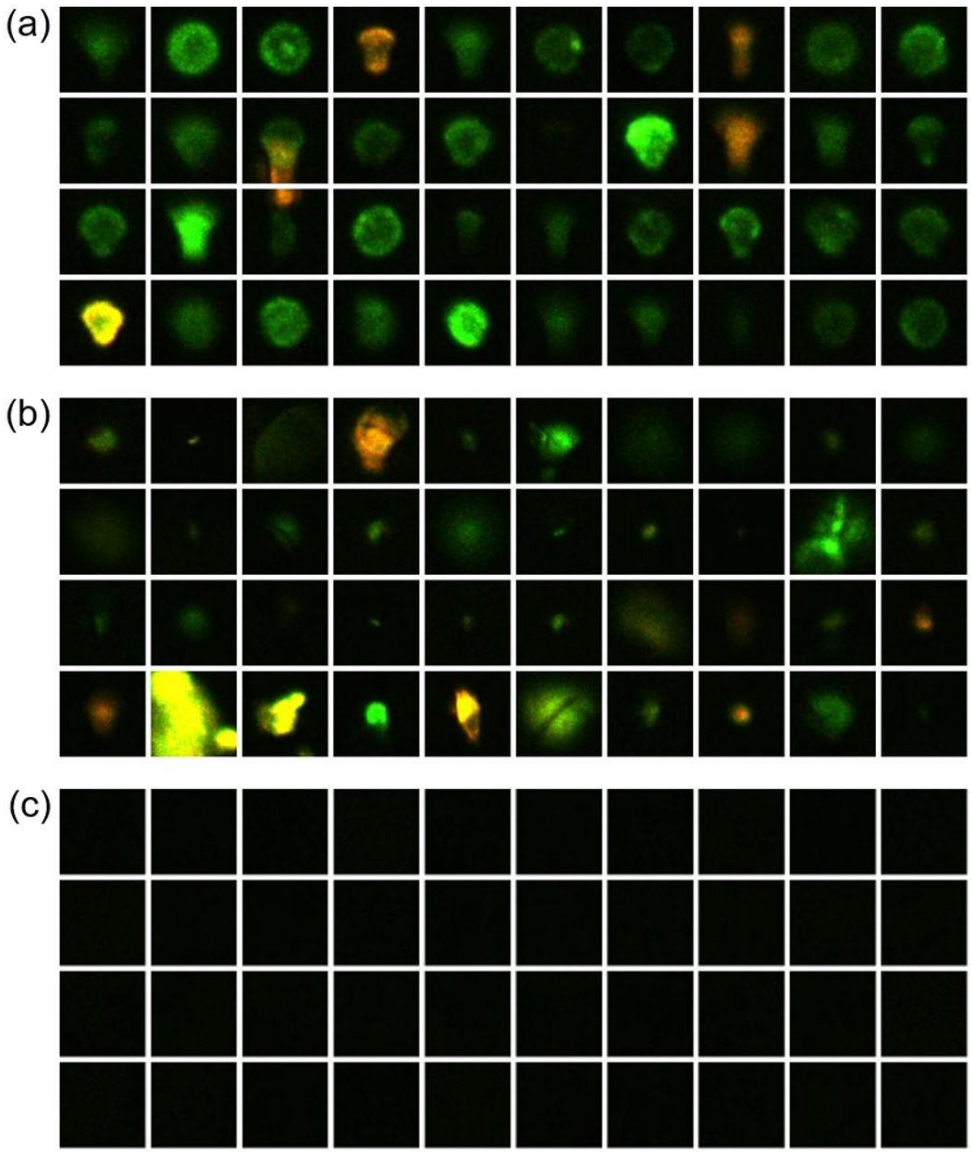

Figure 3.2 Example images from the dataset. (a) Cell images centered and scaled. (b) Hard negative images, that is manually eliminated. (c) Background images.

Cells come in many sizes and shapes since they are deformed by the pillars of the microfluidic chip. To simplify the problem we scaled each cell, so the detector only needs to be trained for the shape information. First a small set of cell images are cropped manually from the training images. This is used to train the initial detector which is then used to automatically

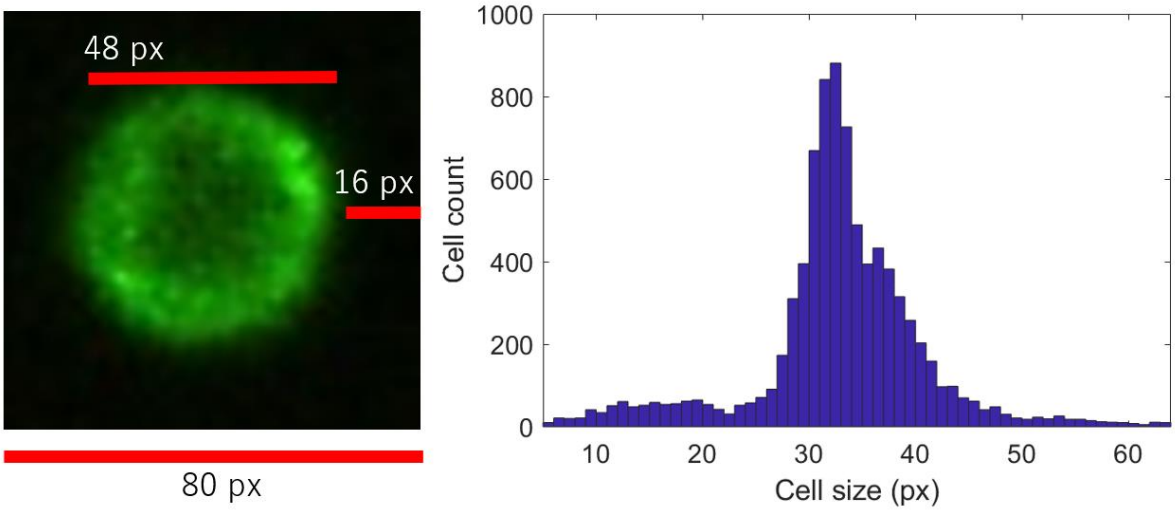

Figure 3.3 Cells are scaled to 48 px in order to keep all the available information, which is decided by the cell size distribution. A band of 16 px around the cells include background information, as background information is crucial for accuracy of detection.

detect and gather training images time effectively. Detected cells are then centered, cropped and scaled. As Figure 3.3 shows the scale of the dataset is important for retaining all the available information. Hence, we decided to scale each cell to 48 px, which is decided by the distribution of cell sizes that we automatically detected. A band of 16 px around the cells include background information which is important for the accuracy of detection [87]. Thus, our detection window size is decided to be 80 px, scaled cell together background band.

Automated process of cell detection, centering, scaling and cropping is the first step in creating the dataset. Unfortunately, the detected cells are not accurately processed, firstly because the initial dataset that we used to automate cell detection is very small, and also for the image processing is likely to fail when there is more than one cell in the cropped region. For those reason the cells are manually checked by an expert to eliminate the misdetections and noises, which are used as hard negatives as Figure 3.2(b) shows. Since looking through

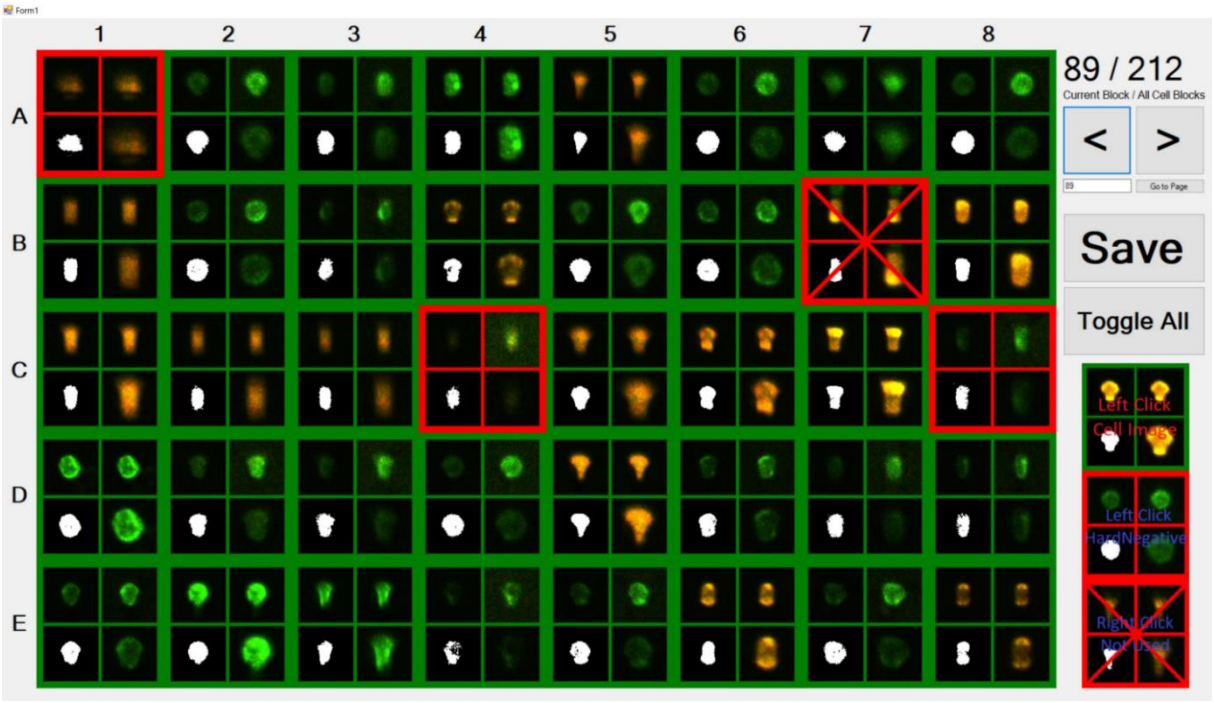

Figure 3.4 Manual identifications of cell by an expert. Green rectangles are chosen as cells, red rectangles are noise/background and crossed red images will be removed from the dataset.

thousands of cell images are not an easy task, a program to ease this laborious work is created for the experts to use. Figure 3.4 displays the graphical user interface (GUI) of the said program. 40 cell images are shown to the expert in each window, as well as the image color normalized image, binary image showing the size of the cell to give an idea about the scaling, and lastly the scaled final image. An expert can look all four images to decide whether to keep it as a cell or mark it as noise which is shown in red rectangles. In case there is a problem with scaling, there are more than a cell or simply unsure about it, they can mark it with crossed in red to remove from the dataset, in which it will not be a part of either cells or background.

50 training images which are dense in cells are annotated manually, also fixing the scaling of the cells when necessary. Another program is supplied to experts, where the cell boundaries are shown to the expert and they can add, remove or change the size of the rectangles. Since

images are large, it is possible to zoom to any area in the image. These annotations are also used to automated creation of negative training samples in different scales. For the accuracy of the detection, these images have to be correctly annotated, even for cell which are weak in fluorescence intensity. For HOG features the intensity of the images are irrelevant, and it is possible to detect even the weakest cells as long as it can be differentiated from the background in terms of weak gradients. For this reason, we supplemented the experts with locally normalized images which is shown in the right of the program GUI in Figure 3.5. For every pixel (x,y) in image I the local normalized image I_n is calculated as,

$$I_n(\mathrm{x},\mathrm{y}) = \frac{I(x,y) - m_I(x,y)}{\sigma_I(x,y)}$$

where $m_I(x,y)$ is an estimation of the local mean of image I around the pixel (x,y). $\sigma_I(x,y)$ is an estimation of the local variance of image I around the pixel (x,y). Normalized images are calculated in MATLAB for simplicity, by convolving the image with gaussian filters to find local mean and variance. The sizes of the filters are empirically chosen, to get a normalized image where cells are easy to differentiate from the background.

Using the dataset generated automatically and annotated by an expert the HOG based detector is trained, then annotated images are exhaustively searched for misdetections. Misdetections are added to the negative dataset which is also called hard negatives. The extended dataset is then used to re-train the final detector.

Emission spectrum crosstalk between the dyes prevents experts from manually labelling the cells as T-cells and B-cells. Hence in order to train the second SVM which identifies T-cells from B-cells, we used the datasets which are only dyed with fluorescence dye. For these images from the single dye experiments, it is possible to label the cells as T-cells or B-cells depending on the dye. These cells are automatically extracted with the final classifier, and only used to train the second SVM with the color features.

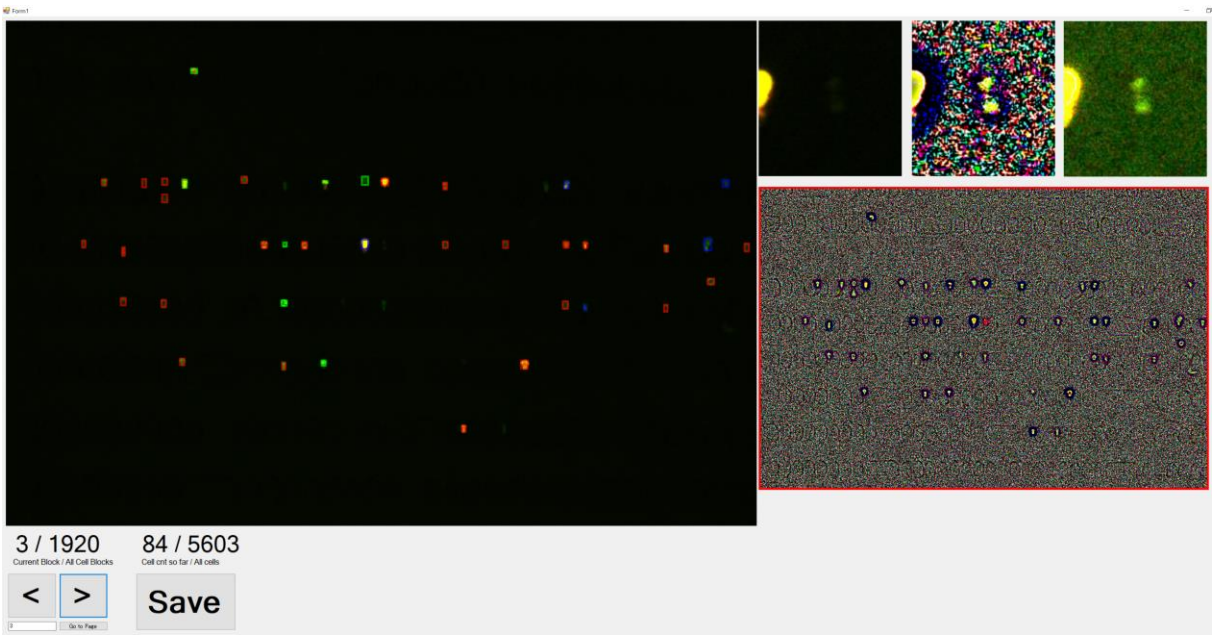

Figure 3.5 Manual additions/corrections of cell by an expert. Cells and noise are annotated by rectangles. On the right, a locally normalized version of the image is supplemented.

3.3 Histogram of Oriented Gradients (HOG)

Preparing the data set appropriately is vital in achieving good performance. Cell images are centered and scaled. Since the size of the cells vary, we upscaled them to 80 pixels squares, with the scaling factor suited to the longest side of the cell bounding boxes. A margin of 16 pixels around the cell on all four sides are included, as this border provides a significant amount of context that facilitates detection. As Figure 3.6 shows, HOG helps us define the shape context of the cells effectively, which in return makes it possible to detect all different shapes of cells deformed by the micropillars in our study.

We computed HOG descriptors for the prepared cell samples. A HOG feature vector is modeled for such an image. Figure 3.7 demonstrates the step by step computation of HOG descriptors. Firstly, one of the image gradient values are determined, to represent the directional changes in

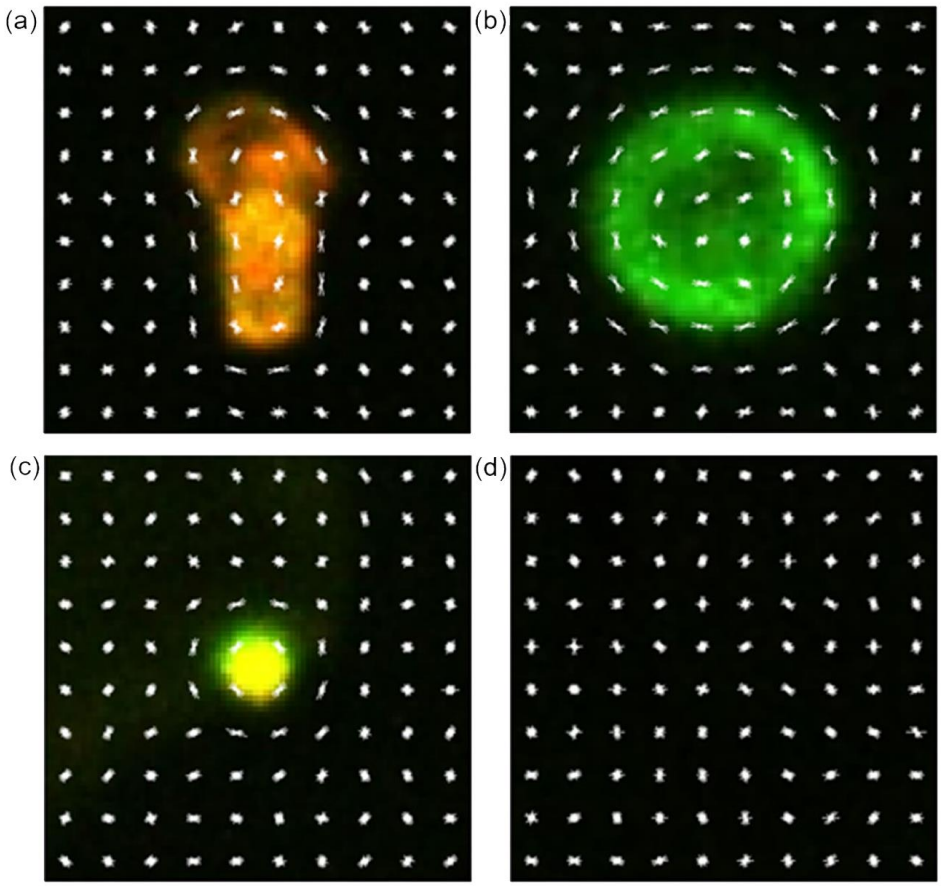

Figure 3.6 (a-b) Histogram of gradient features overlaid on cells, (c) noise and (d) background image

intensity or color. Then the magnitude of the gradient vector is calculated using the partial derivatives of image I in the x and y directions,

$$|\nabla I| = \sqrt{\left(\frac{\partial I}{\partial x}\right)^2 + \left(\frac{\partial I}{\partial y}\right)^2}$$

Next, the gradients in the respective directions are computed through the application of the one dimensional centered, point discrete derivative mask in the horizontal and vertical directions,

$$\frac{\partial I}{\partial x} = I \times [-1 \quad 0 \quad 1],$$

$$\frac{\partial I}{\partial y} = I \times \begin{bmatrix} -1 \\ 0 \\ 1 \end{bmatrix}.$$

The gradient orientations are computed using the vertical and horizontal gradients as,

$$\theta = \tan^{-1}\left(\frac{\partial I}{\partial x} \Big/ \frac{\partial I}{\partial y}\right)$$

Image *I* is then split into cells, and for each cell, a local one dimensional histogram of gradient directions (orientations) is calculated using the pixels from that cell. The histogram channels are evenly spread across 0 to 180 degrees in absolute values and 9 bins were used for the local histogram, thus each histogram bin corresponds to a 20-degree orientation interval. The obtained cell histograms are then merged into a descriptor vector of the image. Firstly, the obtained cell histograms are locally contrast normalized, since the shadowing and illumination in the image may vary. This requires grouping the cells into larger, spatially-connected blocks. After the normalization is conducted, all the histograms can be concatenated in a single feature vector, representing the HOG descriptor. Depending on the cell size and block overlap, the amount of detail one could obtain varies. We used [8x8] cell size to calculate blocks of [16x16] pixels with overlaps using 9 histogram channels. These settings can be regarded as a default choice in object detection. The feature vector of the image is computed as its HOG descriptor, with 2916 coefficients.

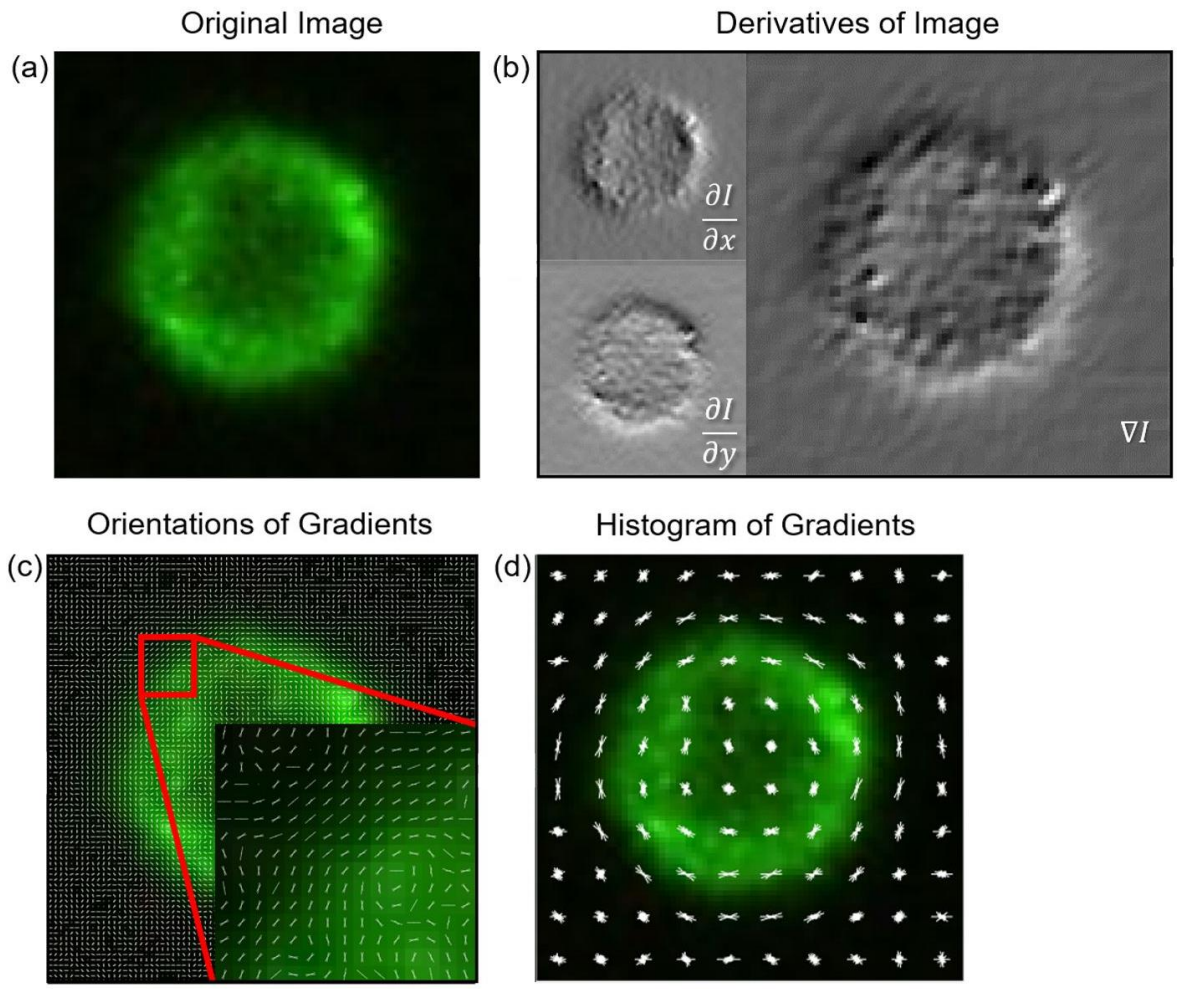

Figure 3.7 (a) Original image, (b) horizontal and vertical derivatives of image, (c) orientations of gradients overlaid on each pixel, (d) orientations gathered into histograms and block normalized

3.4 Color Features

Because the long emission spectrum tail of dyes causes overlap like with the fluorophores FITC and PE, in our T-cells and B-cells counting experiment, cells are stained by a two color (CD3-FITC/CD19-PE) immunofluorescence dye. The color vectors for cells fluctuate in a big range. Cells can be sorted from background and noise through HOG features, but among the detected cells, it is difficult to decide the cell type when taking multicolor cell detection. To

alleviate the influence of fluorescence emission spectrum crosstalk, we calibrated the color distribution of FITC and PE single dye stained cells and then classified dual stained cells by the model trained from single dye stained cells color features. We stained samples with single dye, FITC Mouse Anti-Human CD3 (BD Pharmingen ™, BD Bioscience, San Jose, CA) for T-cells and PE Mouse Anti-Human CD19 (BD Pharmingen ™, BD Bioscience, San Jose, CA) for B-cells. The single dye stained samples were introduced to the same isolation system and sorted under the same condition as dual dye stained sample. As stained by only one fluorescent dye, the detected cells' type could be decided. We used previously trained HOG detector to detect the cells and extracted the average color in RGB space for every cell in FITC and PE. After the cells are detected, an adaptive thresholding using Otsu's method is performed to find the cell segment [89]. Then average color in RGB is calculated using this thresholding as a mask. We trained an RBF kernel SVM using the color averages from single dye stained cells. This calibration needs to be performed only once. Through cross-validation, an average accuracy of 96% was achieved.

3.5 Detection Results

We have created a data set to test the performance of the HOG detector. 500 positive cell images are cropped, centered and scaled from the annotated test images. 50 difficult examples containing noise and 450 randomly selected background examples are used as negative test set. To quantify the HOG detector performance, we plot Receiver Operating Characteristics (ROC's), i.e. true positive rate ($\frac{TruePos}{TruePos+FalseNeg}$) versus false positive rate ($\frac{FalsePos}{FalsePos+TrueNeg}$). Using also this test set we calculated accuracy, specificity and sensitivity values as:

$$\text{Accuracy} = \left(\frac{TruePos + True\ Neg}{Total\ Population}\right)$$

$$\text{Specificity} = \left(\frac{True\ Neg}{TrueNeg + FalsePos}\right)$$

$$\text{Sensitivity} = \left(\frac{TruePos}{TruePos + FalseNeg}\right)$$

In addition to this set of 1,000 image patches, negative images from test data exhaustively searched and around 4,500,000 negative images are added to plot Detection Error Tradeoff (DET) curve on log-log scale i.e. miss rate ($\frac{FalseNeg}{TruePos+FalseNeg}$) versus false positive per window ($\frac{FalsePos}{Total\ Population}$). DET curves present the same information as ROC's but small differences in probabilities are easier to distinguish. Figure 3.8 presents ROC's and DET curves.

Different points in ROC and DET curves corresponds to different accuracy, specificity and sensitivity. We have achieved an accuracy of 94% and sensitivity of 90% when specificity was chosen to be 99%.

In one experiment, 420 frames are scanned for the filtration zone on the microfluidic chip. With the classifiers trained with HOG and color distribution feature, all the 420 images were processed in 67 s with our experiment PC (CPU i7-8700K 3.7 GHz, Nvidia GTX 1080Ti, 64 GB RAM). We have used OpenCV libraries for HOG to perform GPU processing. Figure 3.9 shows the results of an example detection, although cells are of different morphology and size, all cells have been detected.

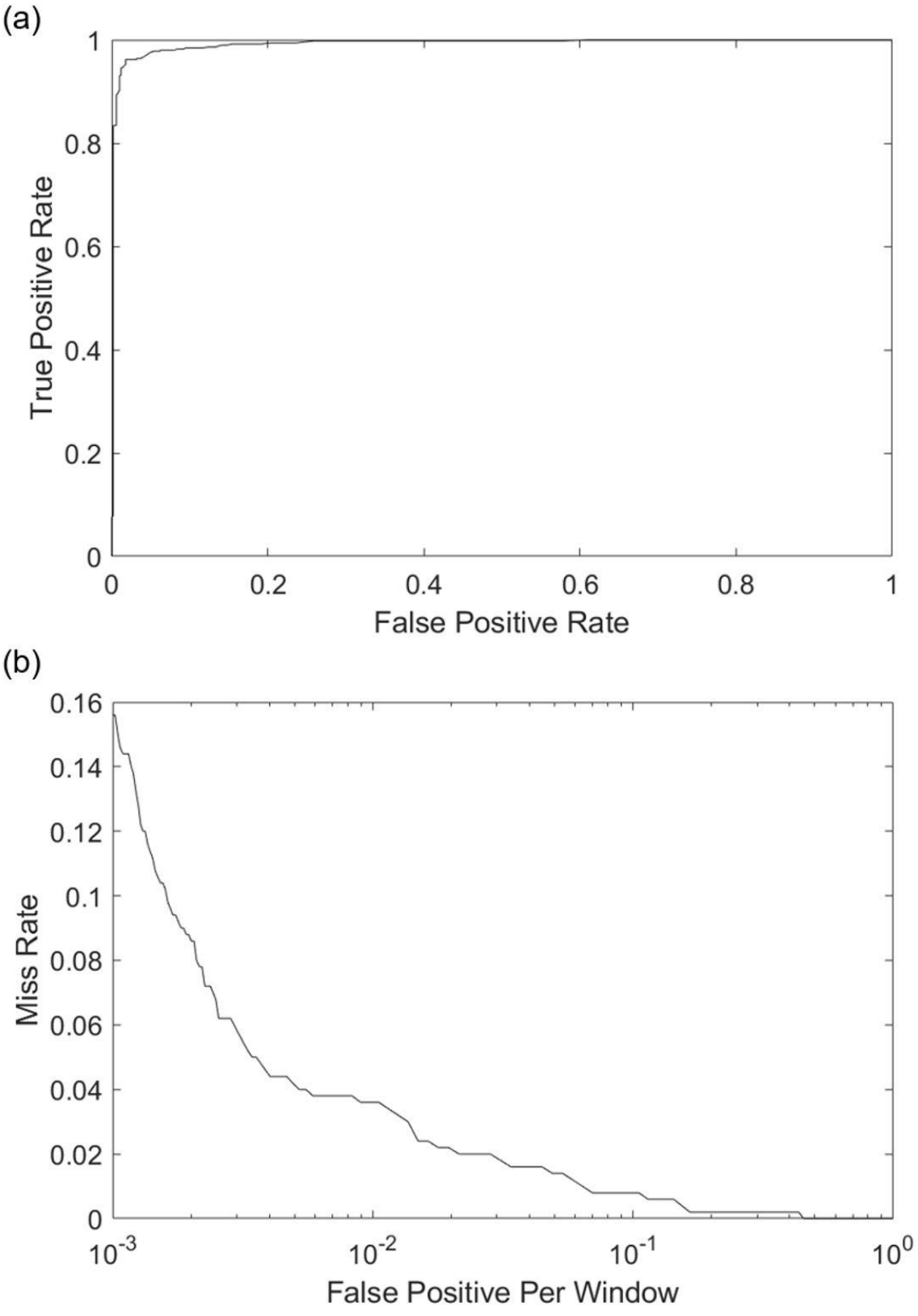

Figure 3.8 (a) ROC and (b) DET curves for HOG detector.

3.6 Summary

Several methods exist for counting the cells in an image [90, 91]. The difficulty of performing the cell segmentation or detection task and choosing the correct algorithm depends much on the type of cells being targeted. If the cells are well separated from each other and have uniform intensity, simple thresholding or watershed algorithms are popular choices of approach. If the cells are packed together, algorithms which account for cell shape and size are preferred [92]. But in our application, the unavoidable uneven illumination over time and across the whole microfluidic chip makes the cells fluorescence intensity differs from image to image. And the cells' shape and size were deformed by pillar structure. The intensity, shape and size features could not be utilized directly to detect cells in our pillar-based microfluidic chip system. Another approach, like the one used in this study, is to recognize cells using training-based machine learning methods. Examples of cells and background are given to the detector, which learns their most important characteristics. Furthermore, to detect both T-cells and B-cells in a single experiment, the emission spectrum crosstalk of these two cells' dyes should also be overcome. In this work, cell detection from fluorescence microscope images is studied using both HOG and color distribution features with SVM learning classifier. HOG features were utilized to distinguish cells from background noise. But HOG features could only distinguish cells from background and noise, how to eliminate the crosstalk between FITC and PE emission spectrum is still a question. We evaluated the color distribution of cells solely stained by FITC or PE and trained the classifier based on the single stained cells' color features. The classifier was used to determine the cell type when sample were stained by dual-color fluorescence (FITC and PE).

In our work, detection of T-cells and B-cells are important in terms of the ratio between them, hence it is more important to have a small ratio of false positives than having a small ratio

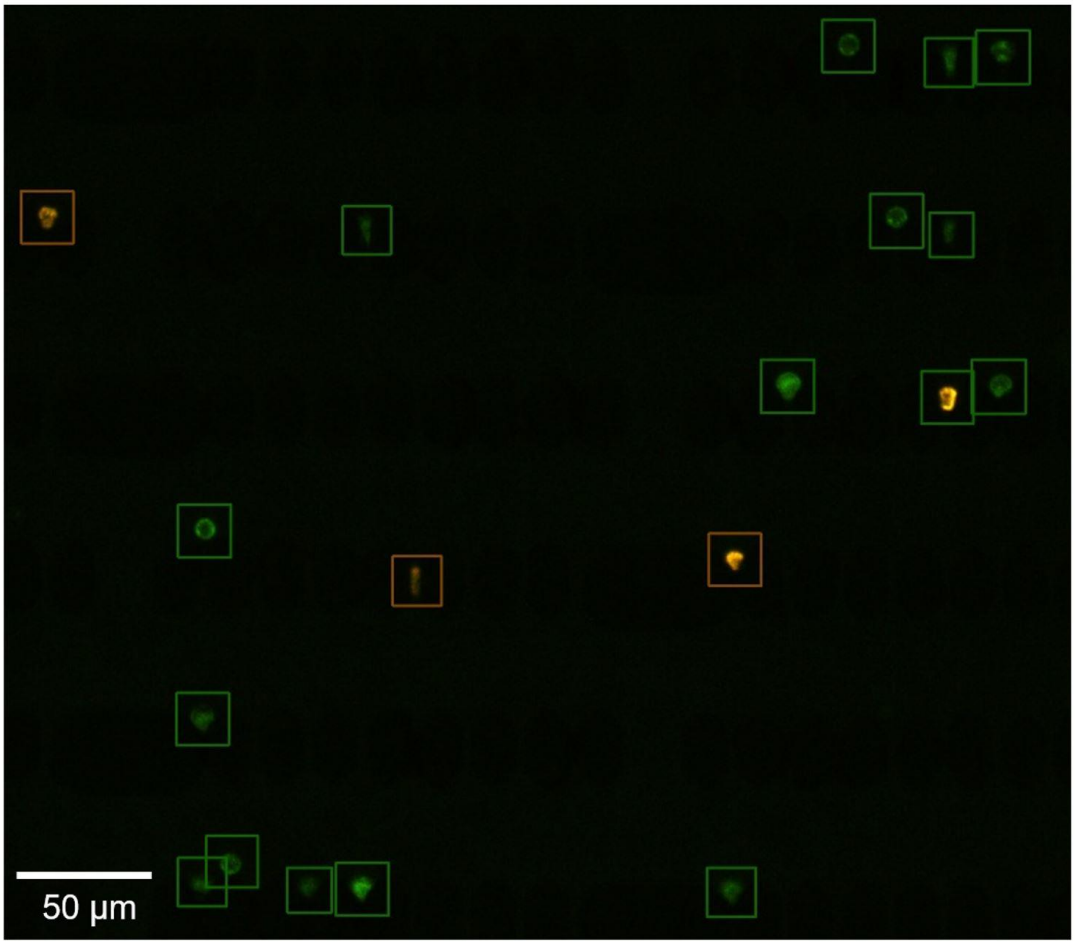

Figure 3.9 Results of counting, a part of the image is cropped for better visibility. The detected T-Cells were labeled with green rectangle and detected B-Cells were labeled with orange rectangle.

of miss rates. Therefore, we set our detector to have less false positives. This is the reason we chose to prioritize having a high enough specificity rate such as 99% while sacrificing accuracy and sensitivity which were 94% and 90% respectively.

Chapter 4.

Improving the Detection of T-cells and B-cells with Deep Learning

4.1 Introduction

As we discussed in the previous chapter, features that can identify the shape of a cell can be extracted by Histogram of Oriented Gradients (HOG) features and this simplifies the classification process by decreasing the amount of sheer data an image holds. But in case of HOG we lose important information such as color data etc. The HOG encompasses the shape of the cells while operating in localized regions and remaining invariant to geometric and photometric transformations. In other words, the HOG can work even when there are

fluctuations in the illumination and shapes of the cells to some extent due to its isolation system design. The HOG can distinguish the cells from the background with a high accuracy rate. However, it might be possible to incorporate features other than shape to increase the accuracy but deciding on what features to use and how to combine them remains an issue.

To get more from an image a key approach is to employ machine learning methods to automate feature extraction, and directly use raw data for classification [93, 94]. Convolutional neural networks (CNNs), train directly on the labeled raw data, and learn the features to be extracted from the images automatically. CNNs are widely used for applications that require object recognition and computer vision such as self-driving cars and face-recognition [95, 96]. CNNs are also used in applications pertaining to cells [97-99]. Despite the attractive qualities of CNNs, they were not widely used for cell detection and classification until recent years, since they require powerful GPUs and large datasets to train. Current GPUs optimized for training CNNs and large datasets containing millions of labeled images such as ImageNet only became available in recent years [100].

4.2 Dataset

In previous chapter we discussed how we created a dataset that contains a total of 6,200 cells and 35,000 background images. We augmented this dataset by using the horizontal reflections of the cell images, then a random subset of background images were chosen for the sake of a better-balanced dataset.

Figure 4.2 illustrates the steps of creating the final dataset and the training of CNNs. Cell images from the experiments in which cells are stained with a single dye were automatically extracted by the proposed CNN and added to the final dataset. These cells were used to calibrate the color distribution and a separate CNN – which will be elaborated on in the following

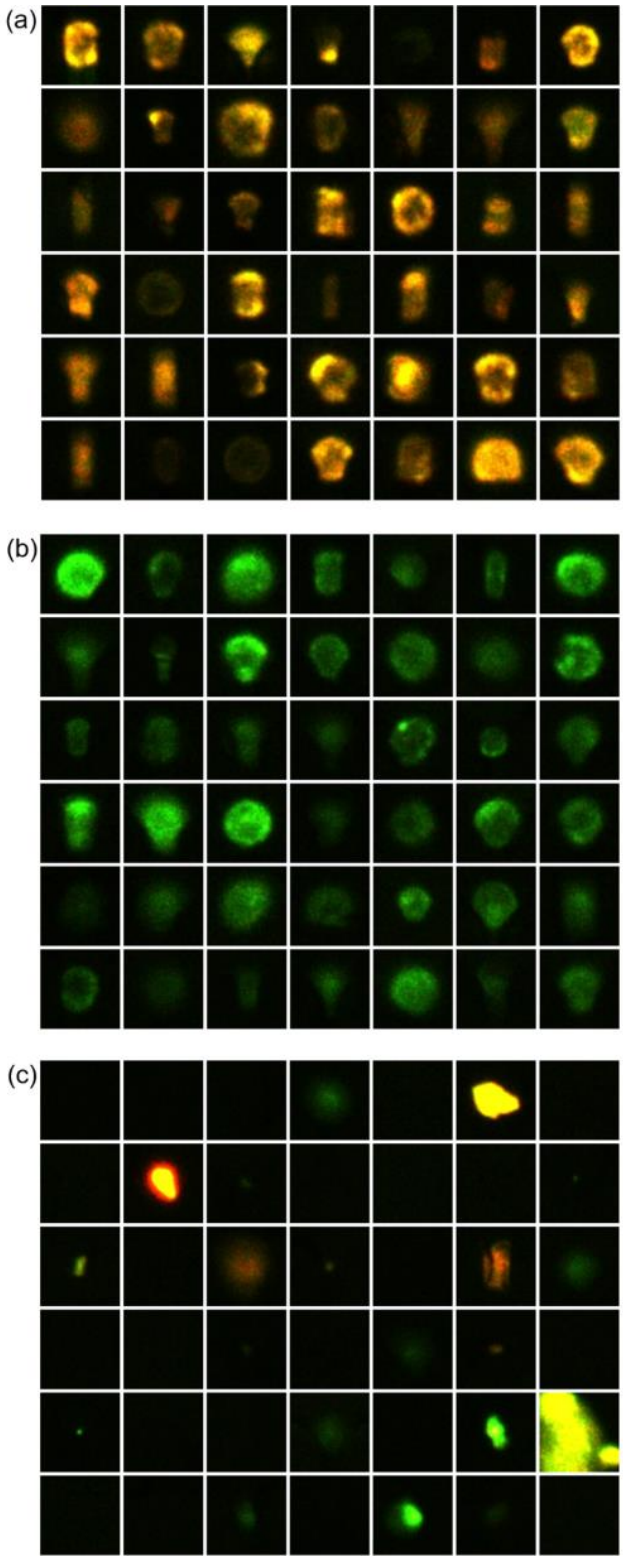

Figure 4.1 Dataset after automated labeling of cells. (a) B-cells, (b) T-cells and (c) background images.

chapters - was trained to distinguish T-Cells from B-Cells. Then using the trained CNN, previously un-annotated cells are annotated. The dataset for training the CNN is finalized with three labels; T-Cell, B-Cell and background as Figure 4.1 demonstrates. The dataset for testing is kept as it is, for the sake of performance comparison.

4.3 Training of Convolutional Neural Network

Figure 4.2 illustrates an artificial neuron and a neural network. The core of a neural network is a neuron which is inspired by a biological neuron. It has weights as parameters that can be learned. It can have many inputs and only one output. The weighted averages of the inputs are calculated then given to the activation function. Depending on this activation function, the output is relayed to the next connected neuron. Neural network is a combination of many neurons as input layer which is connected to hidden layers, and those connected to the final output layer. A neural network is considered a deep neural network if there is more than two hidden layers. It is proven that a neural network with enough complexity can solve any problem [101]. However, neural networks are inefficient with images, simply due to the amount of data an image holds. Convolutional neural networks approximate a fully connected neural network, using the idea that convolutions can capture the spatiality of the images and can decrease the number of parameters a network need to have.

Training a CNN from scratch requires a tremendous amount of data. Although it is possible to re-train a pre-trained CNN using a small dataset which is called transfer learning [102]. It is not always possible to have enough data for a certain application but using data which is in another domain can greatly improve the performance of learning. Transfer training makes use of the already existing CNNs and fine tunes them to the new datasets with a short training time. Many pre-trained CNNs exist like AlexNet [103], VGG [104] and GoogleNet [105]. In this

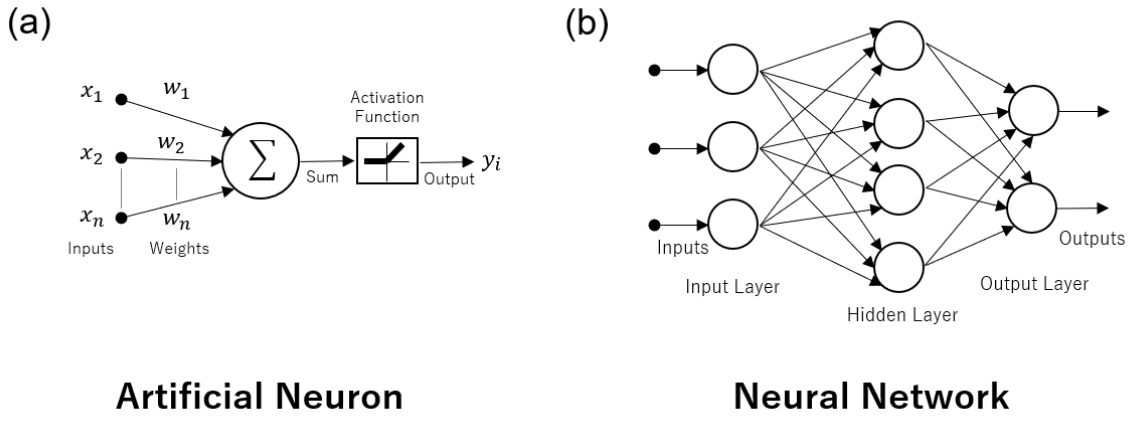

Figure 4.2 (a) An artificial neuron with n inputs, (b) A neural network with one hidden layer.

study we use AlexNet since it is lightweight. Figure 4.3 shows the structure of AlexNet, which takes an image of 227 x 227-px size as input and has five convolutional layers. The last three layers are fully connected, and last layer have 1,000 neurons for the classification of 1,000 classes. It can be thought as the first convolutional layer learns simple color filters, and as we go deeper in the network, layers can emphasize simple shapes, complex shapes and shapes that can be used to define a cell. Only 6% of the parameters of the AlexNet is within the convolutional layers, which is the proof of how efficient convolutional neural networks can be in the sense of number of parameters that needs to be learned.

Transfer learning can be accomplished by removing the last layer of the AlexNet and using the rest of the parameters. AlexNet can classify 1,000 classes but does not include our classes which is T-cell, B-cell and background. So, we replace the last layer of AlexNet according to the number of labels we have. Then using our labelled data, we re-trained the pre-trained CNN. MATLAB's pretrained AlexNet was chosen as a starting point and a stochastic gradient descent with momentum algorithm (with hyperparameters: momentum 0.9, initial learn rate 0.001, max epochs 100, mini batch size 128) was used for re-training. Hyperparameters is crucial for the

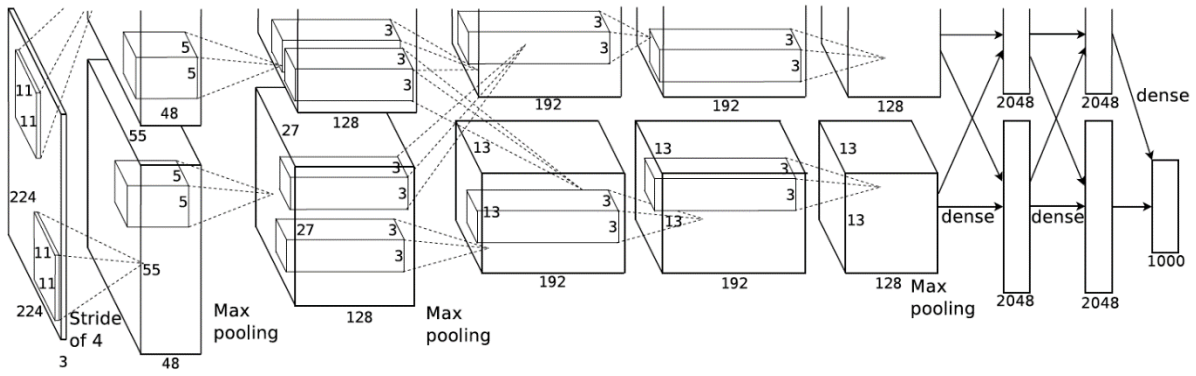

Figure 4.3 The layers of the AlexNet. It is designed to work on two GPUs in parallel, thus the image is split into two GPUs and only in some layers there is connection between GPUs [103].

accurate learn process. Initial learn rate can be changed to accelerate the learning, but it might cause the learning to diverge as well. Mini-batch corresponds to a subset of dataset which from the network's gradients are calculated in each iteration. When all available mini-batches in the dataset is iterated, it is called an epoch, and decides how long training will continue. We have empirically tried many different hyperparameters, but the main point is whether the learning time is enough or if we should train more. Figure 4.4 shows the training process of the MATLAB over a graph of accuracy of each iteration, as the CNN. We can see the accuracy increases, and converges at a point, and no more training is necessary after about 50 epochs. Figure 4.4 (a) is the training graph of 100 epochs while (b) is the training for only 10 epochs. In case of 10 epochs only sensitivity dropped by 1% while accuracy and sensitivity were the same.

Our dataset has around 25,000 training images and we only have three labels: T-Cell, B-Cell and background. Thus, our transfer learned CNN (from here on called AlexCAN: AlexNet based Cell Analyzer Network) has 3 neurons in its last layer.

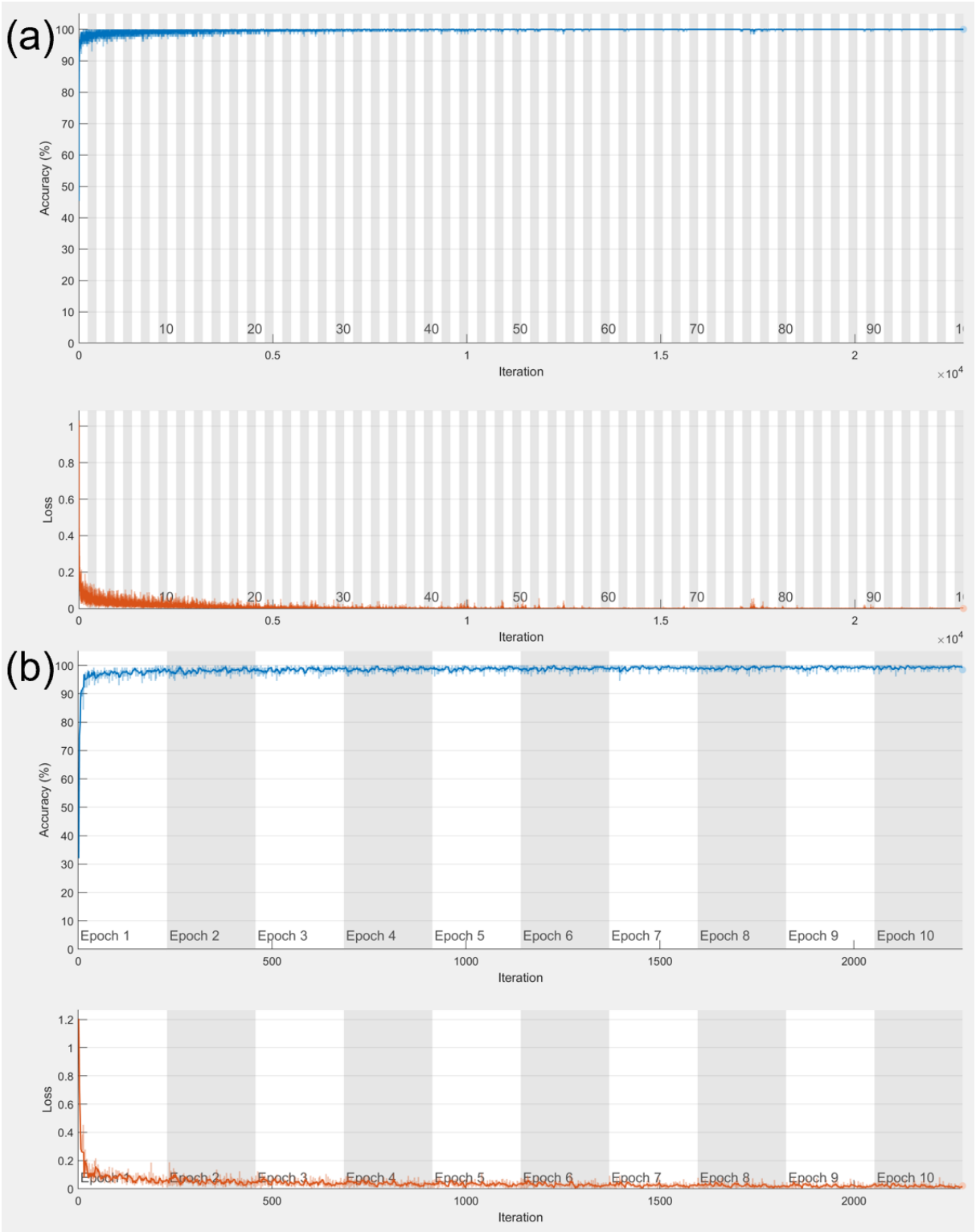

Figure 4.4 Training graphs of CNN. Each white and gray column represents an epoch.

Our dataset that is annotated by an expert does not have annotations for T-cells and B-cells, so it was only labeled as cells and background. We re-trained a CNN which can detect cells from the background as Figure 4.5 shows. Training images were scanned exhaustively by employing the sliding window method to detect cells. We used 3 different scales for the detection window as 64 x 64 pixels, 80 x 80 pixels and 100 x 100 pixels. Since AlexNet requires an input size of 227 x 227 pixels, image patches must be resized before they can be classified. Following the classification of the whole image, multiple detection windows for single cells are combined and weak detections are eliminated.

4.4 Calibrating Color Distribution

In Chapter 3, after the detection of the cells, a color feature-based detector was used to identify cells as T-cells or B-cells respectively. The emission spectrum crosstalk between the dyes prevented us from annotating the cells manually, hence we dyed cells with a single dye, and introduced them to the same isolation system. As they were stained with only one fluorescent dye, the detected cells' type could be determined.

Images from the single dye experiments are used to create a color dataset as Figure 4.2 illustrates. Using the sliding windows method and trained CNN for detection, we created a dataset of 2,300 cells annotated as T-cells and B-cells from 6 experiments and 2,500 images. By using this new dataset, another CNN is re-trained which can separate cells into T-cells and B-cells. A 5-fold cross validation is used to assess the performance. Although this process is straightforward and can be achieved with a simple color feature, we achieved a 99% accuracy rate compared to a 96% accuracy rate from Chapter 3 which used a simpler color feature detector.

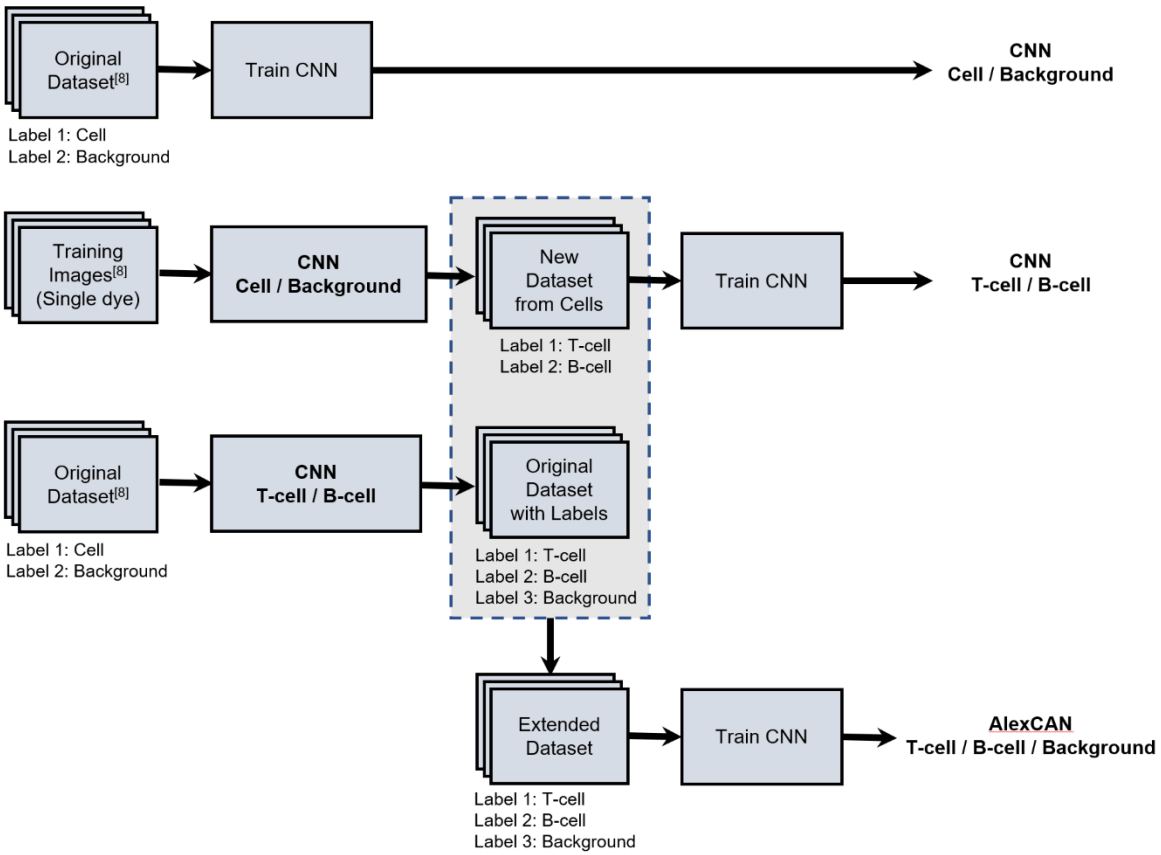

Figure 4.5 Flow chart of training AlexCAN. Firstly, a CNN<Cell/Background> is re-trained using the original dataset and used on training images dyed with a single dye to calibrate color features. After that, another CNN<T-cell/B-cell> is trained from color features, which is used to annotate the original dataset. Lastly AlexCAN is re-trained from the original dataset and the color feature dataset.

Due to the high purity of the detections from the trained CNN and overall accuracy of the automatic annotation, we could add this new dataset to the initial dataset. We also annotated the cells in the initial dataset as T-cells and B-cells using the newly re-trained CNN. This finalized our dataset with three labels as Figure 4.1 illustrates. Using the final dataset AlexCAN is re-trained to detect the cells from the background and this time also annotate them as T-cells and B-cells. Cross validation proved that using the final dataset for AlexCAN can achieve the same

99% accuracy rate for classifying T-cells from B-cells using the color dataset. Moreover, its accuracy in distinguishing cells from the background is also equal to that of the previously re-trained CNN which could detect cells from the background without the type of the cell. Therefore, compared HOG feature based SVM, which we first detected cells from the background and then annotated them as T-cells and B-cells, AlexCAN is simpler.

4.5 Speeding-up by Preselecting Windows using HOG and SVM

AlexCAN has improved performance in terms of identifying T-cells and B-cells and distinguishing them from noise and background. But processing all the images from a single experiment is simply infeasible which requires as much time as 3 days even with the utilization of GPU processing (CPU i7-8700K 3.7 GHz, Nvidia GTX 1080Ti, 64 GB RAM) and efficient implementation (MATLAB – pretrained AlexNet). This is due to the number of detection windows that needs to be classified (in the order of 10^5 for a single image). Moreover every detection window has to be resized to the input size of the AlexCAN. However, even if a smaller CNN with an input size of our detection window is trained, it will still not be fast enough to be used in our application. Hence, we have to reduce the number of detection windows to meet the time requirement of our application.

Due to the design of the chip, cells are sparse on the images. Thus it is possible to reduce the number of detection windows by preselecting them by employing a simpler and faster method. In Chapter 3, we used a HOG features based SVM classifier to detect cells from noise and background. By using HOG features, it is possible to differentiate not only cells but also noise from the background. Hence, we prepared a dataset by coupling cells and noise images together as a positive dataset and used background images as a negative dataset. Figure

4.6 illustrates samples from this new dataset. Using this dataset, the HOG features based SVM classifier is trained.

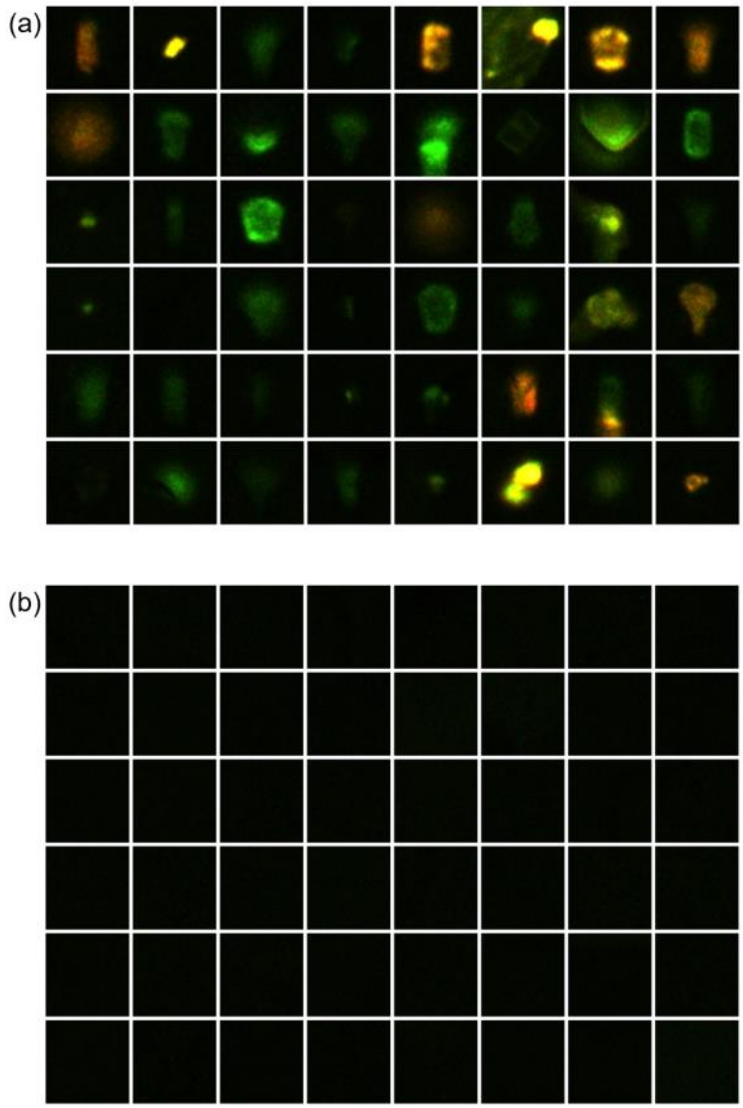

Figure 4.6 Dataset that is tailored to be used for the preselection of detection windows. (a) T-cells, B-cells and noise are all grouped into positive dataset, and (b) the remaining background images are left as negative dataset.

We propose a two-layer classification scheme. At the first layer the HOG features based SVM classifier is used to detect cells and noise from background. The detection windows classified as positive by the HOG features based SVM constitute the preselected windows in our algorithm, and the remaining detection windows will be ignored. In other words, detections from the first classifier are used as input for the second classifier which is AlexCAN. We define the success rate of the HOG features based SVM classifier using the number of cells that are missed. When a cell is not within any preselected window, we count it as a miss. Figure 4.7 demonstrates the miss rate of cells by the first classifier versus the percentage of the preselected windows i.e. the ratio of preselected windows to all the detection windows. The miss rate decreases as the percentage of preselected windows increases. The processing time of AlexCAN increases linearly with the increasing of the percentage of the preselected windows, hence the miss rate has a lower bound depending on our time requirement.

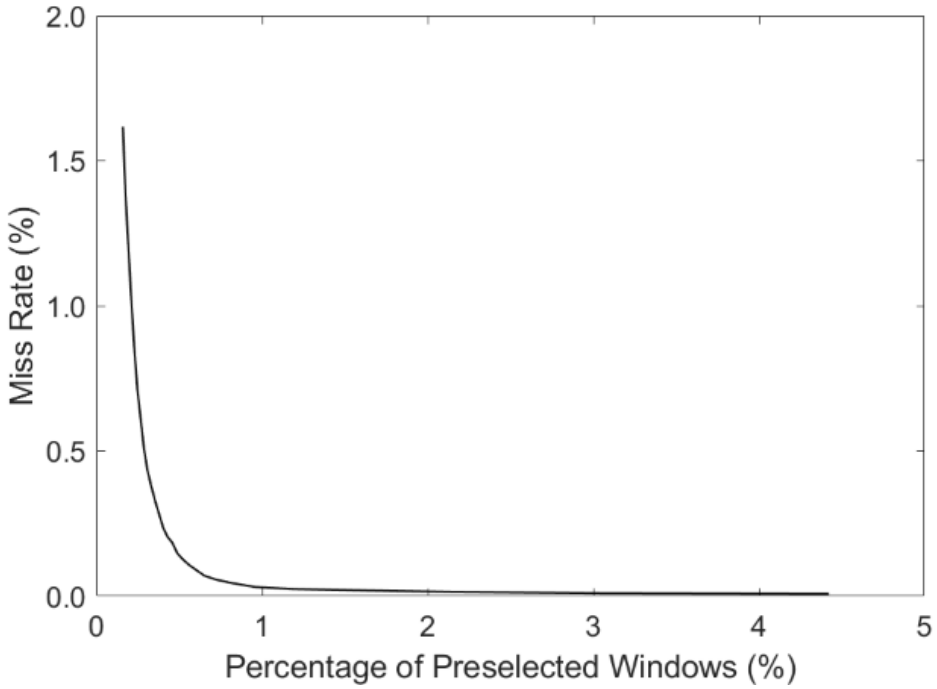

Figure 4.7 Miss rate of the HOG features based SVM when preselecting windows for AlexCAN.

Figure 4.8 illustrates this process flow, with an example image. Input images are first preprocessed by the HOG features based SVM classifier. Using the sliding windows approach, the images are scanned using three different scales as 64 x 64 pixels, 80 x 80 pixels and 100 x 100 pixels. Figure 4.8 (b) shows the preselected windows which are the output of the first classification layer. The preselected windows are resized to the input size of AlexCAN and then each preselected window is classified as T-cell, B-cell and background. The detections from T-cells and B-cells are grouped separately, and weak windows are eliminated.

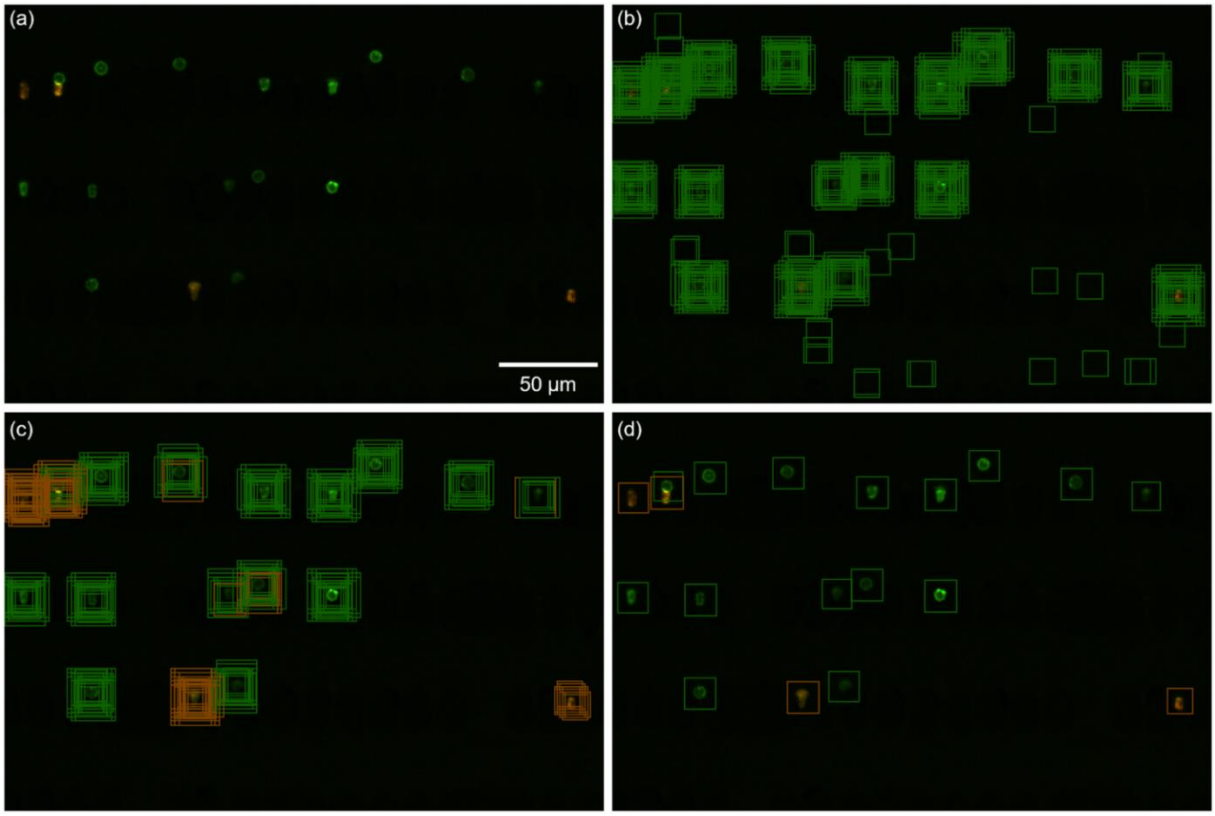

Figure 4.8 (a) Original image. (b) Green rectangles show preselected windows by the HOG features based SVM classifier, (c) classification results by AlexCAN; green rectangles show detection windows that are classified as T-cells and orange rectangles show detection windows that are classified as B-cells and (d) final result after grouping the detection windows.

4.6 Detection Results

We used the same test set from chapter 3, in order to compare performance. 500 positive cell images were cropped, centered and scaled from the annotated test images. 50 complex examples containing noise and 450 randomly selected background examples were used as negative test set. To quantify the performance of the detectors we plotted the Receiver Operating Characteristics (ROC's), *i.e.* true positive rate ($\frac{TruePos}{TruePos+FalseNeg}$) versus false positive rate ($\frac{FalsePos}{FalsePos+TrueNeg}$). Also using this test set we calculated accuracy, specificity and sensitivity values as:

$$\text{Accuracy} = \left(\frac{TruePos + True\ Neg}{Total\ Population}\right)$$

$$\text{Specificity} = \left(\frac{True\ Neg}{TrueNeg + FalsePos}\right)$$

$$\text{Sensitivity} = \left(\frac{TruePos}{TruePos + FalseNeg}\right)$$

In addition to this set of 1,000 image patches, negative images from the test data were exhaustively searched and around 4,500,000 negative images were added to the plot Detection Error Tradeoff (DET) curve on a log-log scale i.e. miss rate ($\frac{FalseNeg}{TruePos+FalseNeg}$) versus false positive per window ($\frac{FalsePos}{Total\ Population}$). The DET curves present the same information as the ROC's but small differences in probabilities are easier to distinguish. We presented the performance of three different cases. In the first case AlexCAN was used to classify the image by employing the sliding window method. In the second case detection windows were preselected using the HOG features based SVM classifier to be used with AlexCAN. The last case was our previous work to provide a performance comparison between our previos work and AlexCAN and AlexCAN using preselected windows.

Figure 4.9 presents the ROC's and DET curves for the three different cases. The different points in the ROC's and DET curves correspond to different rates of accuracy, specificity and sensitivity. We achieved an accuracy of 98%, sensitivity of 97% and specificity of 99% in both cases using AlexCAN and AlexCAN using preselected windows, compared to the accuracy of 94%, sensitivity of 90% and specifity of 99% of HOG based SVM classifier we have introduced in Chapter 3.

In one experiment, a total of 420 images were scanned for the filtration zone on the microfluidic chip. Preselecting windows via the HOG feature based SVM classifier takes about 20 secs for 420 images. Classifying preselected windows with AlexCAN takes less than 10 min with our experiment PC. We used OpenCV libraries for the HOG features to perform GPU processing and MATLAB for AlexCAN.

4.7 Summary

In chapter 3, the HOG features were utilized to distinguish cells from background and noise. However, the HOG features only use shape information, and other features such as color and texture are omitted. In blood analysis system we propose, the estimation of the ratio of T-cells and B-cells have utmost priority, so we chose to have a specificity rate as high as 99% and hence sacrificing the accuracy and sensitivity rate which were 94% and 90% respectively. This is a result of the HOG features is very good, but it still has room to improve.

We trained a pre-trained CNN employing transfer learning in order to address the low sensivity. Owing to optimized feature kernels that are trained using an image dataset in the order of millions, the pre-trained AlexNet enables a great improvement in performance compared to the HOG features based SVM classifier. Transfer learning makes it possible to apply a pre-trained network to a new domain such as T-cell and B-cell detection with a dataset only in the

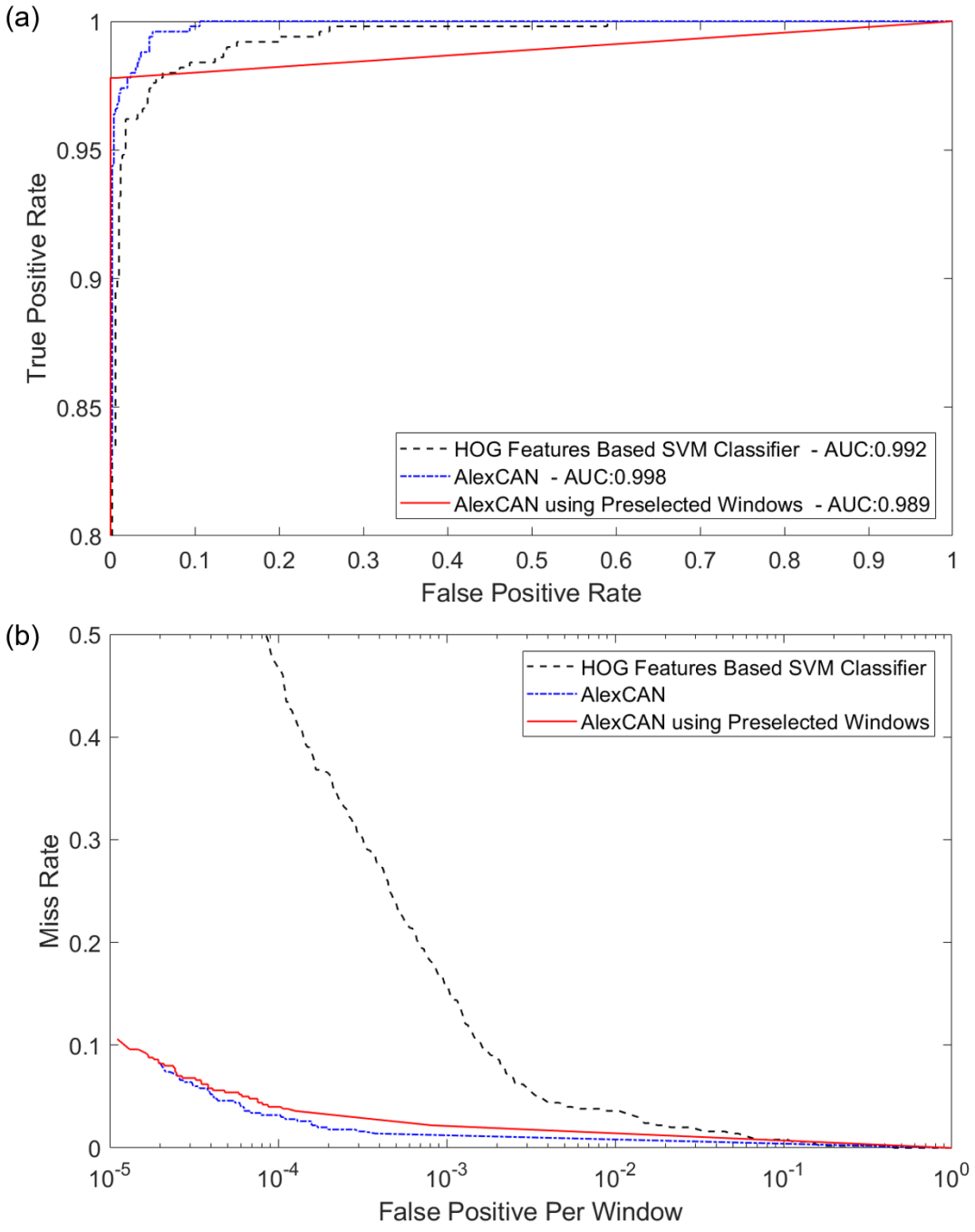

Figure 4.9 (a) ROC's curves for three different cases are presented along with the area under curves (AUC). The performance of AlexCAN is clear through the ROC's curve and AUC. In the case of using preselected windows ROCs only includes preselected windows thus it starts from a high true positive rate, but does not increase with increasing false positive rate, hence

the AUC of it is smaller. (b) DET curves which are similar to ROC's provide a better comparison.

order of thousands. With AlexCAN we achieved an accuracy of 98%, sensitivity of 97% and specificity of 99%. Even though recent advances in GPU architecture rendered it possible to train CNNs as large as ours, using the sliding window method and classifying all the windows in every image from an experiment is time consuming.

Increasing the speed for our application is crucial. However using a better GPU or training a smaller and faster CNN is unfortunately not the answer. We need an increase in speed in the order of hundreds, and we proposed a method to preselect detection windows. By reducing the number of windows to be classified, the total time for detection was reduced from about 3 days to 10 mins which is almost 500 times faster. This method might miss some cells, but looking at our results, the total time required for detection is down to feasible levels. As Figure 4.8 (d) shows, AlexCAN using preselected windows can detect all the cells despite their varying morphology and size.

Chapter 5.

Conclusion and Future Works

5.1 Summary

In this thesis we presented a blood analysis system for the isolation and detection of T-cells and B-cells using a pillar-based microfluidic chip. The leukocytes are isolated from whole blood using gradual filtering by the microfluidic chip and via immunofluorescence imaging the T-cells and B-cells are detected automatically by employing machine learning methods. The proposed method and system could also be applied to all other specific leukocytes using different fluorescent dyes.

In chapter 2, the microfluidic chip design and isolation of the leukocytes are discussed in detail. A micro-pillar array based gradual filtering is proposed, and anti-clogging strategies such as adding escape routes to the microfluidic chip design are proposed. The microfluidic chip design is accomplished through many empirical trial and errors. The microfluidic chip can be fabricated using soft lithography, first a mold is created by photolithography from photoresist that is spin coated on a silicon wafer, then PDMS is molded and bonded with glass through plasma treatment. Thus, it is ensured and confirmed that our chip is clog-free. Using the microfluidic chip, a trap rate of 99.8% is achieved. Lastly, we discussed the system configuration in which the autonomous scan of filtration zone of the microfluidic chip is made possible, and the images acquired are sent to the image analysis for detection.

In Chapter 3, a Histogram of Oriented Gradients (HOG) and color features based SVM classifier was proposed to overcome the difficulties in the cell detection process, such as fluorescence emission spectrum crosstalk, variability of cell size and morphology, differences in illumination and inconsistence fluorophores expressing level on living cells. We performed numerous cell detection experiments using the detection technique provided. The experiment tests performed on various image datasets, have produced satisfactory detection results that prove the effectiveness of our proposed approach. It has achieved a high accuracy of 94%, specificity of 99% and sensitivity of 90%. For T-cells B-cells detection we have achieved 96% cross-validation accuracy. Image analysis requires about 67 secs for a single experiment.

In Chapter 4, a deep convolutional neural network classifier is trained to detect and classify T-cells and B-cells. The experiments performed on various image datasets, have produced satisfactory detection results that prove the effectiveness of our proposed approach. We achieved a high accuracy of 98%, specificity of 99% and sensitivity of 97%. For T-cells and B-cells detection we achieved a 99% cross-validation accuracy rate. AlexNet based cell network analyser's (AlexCAN's) performance is found to be better compared to HOG features based

SVM classifier (accuracy of 94%, specificity of 99% and sensitivity of 90%). However, CNNs require more time compared to the simple HOG features based SVM classifier, and it is infeasible for practical use. Hence, we proposed a two-layer classification method to accelerate detection, we first use a HOG based SVM classifier to preselect windows to be classified by AlexCAN. Using AlexCAN with preselected windows, we achieved the same accuracy rate of 98%, specificity of 99% and sensitivity of 97%. Preselecting windows with HOG based SVM requires 20 secs and AlexCAN requires 10 mins to classify the preselected windows.

The blood analysis system has a high capture rate of leukocytes as high as 99.8% using the microfluidic chip. Combined with the 98% detection accuracy of T-cells and B-cells our proposed system can effectively and accurately isolate and count T-cells and B-cells from a small volume of whole blood.

5.2 Future Works

5.2.1 Integration and Improvement of the Blood Analysis System

As a point-of-care standalone blood analysis system, our work is far from complete. We will continue to improve to make it more efficient, smaller in size and cheaper in cost. As a parallel research rare cell isolation from open microfluidic chip also continues. Using the same system, and different microfluidic chips, we would like to make the blood analysis system to have multiple uses in research centers and clinical laboratories all around the world.

Our short-term work is the integration of the proposed machine learning algorithms to the blood analysis system. The machine learning detection of T-cells and B-cells are completed using a different PC after the complete scan of the filtration zone. This means, the images first have to be saved into the hard-drive of the PC and then need to be loaded again before the detection algorithms could be used. Although it is not vital to integrate the detection into the

blood analysis system, it is possible to detect and count T-cells and B-cells in parallel with the automated scanning of the microfluidic chip. This way the time requirement for the scan and detection would be significantly reduced.

And lastly, we are currently in the middle of an upgrade of the blood analysis system. The main body of the blood analysis system is designed again to make it smaller and to increase the functionality with the addition of the new components. It will be possible to further automate the isolation and scanning process with position calibration and auto focusing of the microscope. A new user interface and automation system needs to be implemented for the new blood analysis system, as well as the integration of the machine learning algorithms we proposed.

5.2.2 Point-of-Care Blood Analysis System

Roughly 37 million people worldwide are infected with HIV, the disease burden is the highest in resource limited settings. The $CD4^+$ T-cell count is a critical test in the management of HIV and is widely used to determine when to initiate antiretroviral therapy and to monitor the efficacy of treatment [28]. Flow cytometry is the standard diagnostic method for T-cells counting, but it requires centralized laboratory facilities and trained personnel, which is simply not possible to afford for poverty-stricken regions. Point-of-care blood analysis systems that are being developed are expected to eliminate the socioeconomic or geographic barriers that currently prevent access to two-thirds of HIV-infected people in resource limited settings such as Sub-Saharan Africa [106].

The blood analysis system we have proposed in this thesis, can rapidly and accurately separate and count T-cells from the whole blood. We hope our system will be used as a point-of-care diagnosis of many diseases, which is otherwise costly and time consuming. Microfluidic chips are inexpensive and disposable, and we believe our system would be affordable even in

resource limited regions. For this purpose, our future work is the completion and commercialization of the blood analysis system that we have proposed.

References

[1] McGuill, M.W. and A.N. Rowan, *Biological effects of blood loss: implications for sampling volumes and techniques.* ILAR Journal, 1989. **31**(4): p. 5-20.

[2] Blausen.com, *Medical gallery of Blausen Medical 2014.* WikiJournal of Medicine, 2014. **1**(2): p. 10.

[3] Jandl, J.H., *Blood: Textbook of Hematology*. 1996, Boston: Little Brown, 2nd edition. 1510.

[4] Conquer, J.A., et al., *Fatty acid analysis of blood plasma of patients with Alzheimer's disease, other types of dementia, and cognitive impairment.* Lipids, 2000. **35**(12): p. 1305-1312.

[5] Geyer, P.E., et al., *Plasma proteome profiling to assess human health and disease.* Cell systems, 2016. **2**(3): p. 185-195.

[6] Thomas, J., *Plasma viscosity as a routine laboratory test.* Journal of clinical pathology, 1978. **31**(3): p. 293.

[7] Li, F.P., B.P. Alter, and D.G. Nathan, *The mortality of acquired aplastic anemia in children.* Blood, 1972. **40**(2): p. 153-162.

[8] Perrotta, S., P.G. Gallagher, and N. Mohandas, *Hereditary spherocytosis.* The Lancet, 2008. **372**(9647): p. 1411-1426.

[9] Camaschella, C., *Iron-deficiency anemia.* New England journal of medicine, 2015. **372**(19): p. 1832-1843.

[10] Vincent, J.L., et al., *Anemia and blood transfusion in critically ill patients.* Jama, 2002. **288**(12): p. 1499-1507.

[11] Serjeant, G.R. and B.E. Serjeant, *Sickle cell disease*. Vol. 3. 1992: Oxford university press New York.

[12] Beier, J.C., *Malaria parasite development in mosquitoes.* Annual review of entomology, 1998. **43**(1): p. 519-543.

[13] Tefferi, A., et al., *Proposals and rationale for revision of the World Health Organization diagnostic criteria for polycythemia vera, essential thrombocythemia, and primary myelofibrosis: recommendations from an ad hoc international expert panel.* Blood, 2007. **110**(4): p. 1092-1097.

[14] Cines, D.B. and V.S. Blanchette, *Immune thrombocytopenic purpura.* New England Journal of Medicine, 2002. **346**(13): p. 995-1008.

[15] Kakkar, V., et al., *Natural history of postoperative deep-vein thrombosis.* The Lancet, 1969. **294**(7614): p. 230-233.

[16] Maton, A., *Human biology and health*. 1997: Prentice Hall.

[17] Kabra, S., et al., *Multidrug-resistant typhoid fever.* Tropical doctor, 2000. **30**(4): p. 195-197.

[18] Hummer, M., et al., *Transient neutropenia induced by clozapine.* Psychopharmacology bulletin, 1992. **28**(3): p. 287-290.

[19] Shankar, A., et al., *Association between circulating white blood cell count and cancer mortality: a population-based cohort study.* Archives of internal medicine, 2006. **166**(2): p. 188-194.

[20] Grimm, R.H., J.D. Neaton, and W. Ludwig, *Prognostic importance of the white blood cell count for coronary, cancer, and all-cause mortality.* Jama, 1985. **254**(14): p. 1932-1937.

[21] Dudley, M.E., et al., *Cancer regression and autoimmunity in patients after clonal repopulation with antitumor lymphocytes.* Science, 2002. **298**(5594): p. 850-854.

[22] Dias, A.M.B., et al., *White Blood Cell Count Abnormalities and Infections in One-year Follow-up of 124 Patients with SLE.* Annals of the New York Academy of Sciences, 2009. **1173**(1): p. 103-107.

[23] Hunninghake, G.W. and R.G. Crystal, *Cigarette smoking and lung destruction: accumulation of neutrophils in the lungs of cigarette smokers.* American Review of Respiratory Disease, 1983. **128**(5): p. 833-838.

[24] Blay, J., et al., *Early lymphopenia after cytotoxic chemotherapy as a risk factor for febrile neutropenia.* Journal of Clinical Oncology, 1996. **14**(2): p. 636-643.

[25] Costa, S., et al., *B-cell and T-cell quantification in minor salivary glands in primary Sjögren's syndrome: development and validation of a pixel-based digital procedure.* Arthritis research & therapy, 2016. **18**(1): p. 21.

[26] Bernal, E., et al., *The CD4: CD8 ratio is associated with IMT progression in HIV-infected patients on antiretroviral treatment.* Journal of the International AIDS Society, 2014. **17**: p. 19723.

[27] Sweiss, N.J., et al., *Significant CD4, CD8, and CD19 lymphopenia in peripheral blood of sarcoidosis patients correlates with severe disease manifestations.* PLoS One, 2010. **5**(2): p. e9088.

[28] Watkins, N.N., et al., *Microfluidic CD4+ and CD8+ T lymphocyte counters for point-of-care HIV diagnostics using whole blood.* Science translational medicine, 2013. **5**(214): p. 214ra170-214ra170.

[29] Barnett, D., et al., *CD4 immunophenotyping in HIV infection.* Nature Reviews Microbiology, 2008. **6**(11supp): p. S7.

[30] Serrano-Villar, S., et al., *The CD 4: CD 8 ratio is associated with markers of age-associated disease in virally suppressed HIV-infected patients with immunological recovery.* HIV medicine, 2014. **15**(1): p. 40-49.

[31] Verso, M., *The evolution of blood-counting techniques.* Medical history, 1964. **8**(2): p. 149-158.

[32] Buttarello, M. and M. Plebani, *Automated Blood Cell CountsState of the Art.* American Journal of Clinical Pathology, 2008. **130**(1): p. 104-116.

[33] Coulter, W.H. *High speed automatic blood cell counter and cell size analyzer*. in *Proceedings of the National Electronics Conference*. 1956.

[34] Piyasena, M.E. and S.W. Graves, *The intersection of flow cytometry with microfluidics and microfabrication.* Lab on a Chip, 2014. **14**(6): p. 1044-1059.

[35] Kamentsky, L.A., M.R. Melamed, and H. Derman, *Spectrophotometer: new instrument for ultrarapid cell analysis.* Science, 1965. **150**(3696): p. 630-631.

[36] Kamentsky, L.A. and M.R. Melamed, *Spectrophotometric cell sorter.* Science, 1967. **156**(3780): p. 1364-1365.

[37] Sabban, S., *Development of an in vitro model system for studying the interaction of Equus caballus IgE with its high-affinity FcεRI receptor*. 2011, University of Sheffield.

[38] Hassan, U., et al., *A microfluidic biochip for complete blood cell counts at the point-of-care.* Technology, 2015. **3**(04): p. 201-213.

[39] Keeney, M., B. Hedley, and I. Chin-Yee, *Flow cytometry—recognizing unusual populations in leukemia and lymphoma diagnosis.* International journal of laboratory hematology, 2017. **39**: p. 86-92.

[40] Abraham, R.S. and G. Aubert, *Flow Cytometry: A Versatile Tool For Diagnosis And Monitoring Of Primary Immunodeficiencies (PIDs).* Clinical and Vaccine Immunology, 2016: p. CVI. 00001-16.

[41] ThermoFisherScientific. *Attune NxT Flow Cytometer*. 2018 [cited 2018 Dec 17]; Available from: https://www.thermofisher.com.

[42] Huang, X., et al., *A contact-imaging based microfluidic cytometer with machine-learning for single-frame super-resolution processing.* PloS one, 2014. **9**(8): p. e104539.

[43] El-Ali, J., P.K. Sorger, and K.F. Jensen, *Cells on chips.* Nature, 2006. **442**(7101): p. 403.

[44] Shields IV, C.W., C.D. Reyes, and G.P. López, *Microfluidic cell sorting: a review of the advances in the separation of cells from debulking to rare cell isolation.* Lab on a Chip, 2015. **15**(5): p. 1230-1249.

[45] Wu, H.-W., et al., *An integrated microfluidic system for isolation, counting, and sorting of hematopoietic stem cells.* Biomicrofluidics, 2010. **4**(2): p. 024112.

[46] Agarwal, S., et al., *Formation of embryoid bodies using dielectrophoresis.* Biomicrofluidics, 2012. **6**(2): p. 024101.

[47] Hoi, S.-K., et al., *Passive optical separation and enrichment of cells by size difference.* Biomicrofluidics, 2010. **4**(4): p. 044111.

[48] Kim, Y., S.H. Lee, and B. Kim, *Droplet-based magnetically activated cell separation: analysis of separation efficiency based on the variation of flow-induced circulation in a pendent drop.* Analytical and bioanalytical chemistry, 2009. **395**(7): p. 2415-2421.

[49] Nam, J., et al., *Density-dependent separation of encapsulated cells in a microfluidic channel by using a standing surface acoustic wave.* Biomicrofluidics, 2012. **6**(2): p. 024120.

[50] Liu, Y., D. Hartono, and K.-M. Lim, *Cell separation and transportation between two miscible fluid streams using ultrasound.* Biomicrofluidics, 2012. **6**(1): p. 012802.

[51] Masuda, T., et al., *Rare cell isolation and recovery on open-channel microfluidic chip.* PloS one, 2017. **12**(4): p. e0174937.

[52] Hosokawa, M., et al., *Leukocyte counting from a small amount of whole blood using a size-controlled microcavity array.* Biotechnology and bioengineering, 2012. **109**(8): p. 2017-2024.

[53] Alvankarian, J., A. Bahadorimehr, and B. Yeop Majlis, *A pillar-based microfilter for isolation of white blood cells on elastomeric substrate.* Biomicrofluidics, 2013. **7**(1): p. 014102.

[54] Hulspas, R. and J. Bauman, *The use of fluorescent in situ hybridization for the analysis of nuclear architecture by confocal microscopy.* Cell biology international reports, 1992. **16**(8): p. 739-747.

[55] Basiji, D.A., et al., *Cellular image analysis and imaging by flow cytometry.* Clinics in laboratory medicine, 2007. **27**(3): p. 653-670.

[56] Orchard, J.A., et al., *ZAP-70 expression and prognosis in chronic lymphocytic leukaemia.* The Lancet, 2004. **363**(9403): p. 105-111.

[57] Brasko, C., et al., *Intelligent image-based in situ single-cell isolation.* Nature communications, 2018. **9**(1): p. 226.

[58] Anselmetti, D., *Single cell analysis: technologies and applications*. 2009: John Wiley & Sons.

[59] Caicedo, J.C., et al., *Data-analysis strategies for image-based cell profiling.* Nature methods, 2017. **14**(9): p. 849.

[60] Standage, T., *The mechanical Turk: the true story of the chess-playing machine that fooled the world*. 2002: Allen Lane The Penguin Press.

[61] Newborn, M., *Kasparov versus Deep Blue: Computer chess comes of age*. 2012: Springer Science & Business Media.

[62] Hodges, A., *Alan Turing and the Turing machine.* The Universal Turing Machine a Half-Century Survey, 1995: p. 3-14.

[63] Shipp, M.A., et al., *Diffuse large B-cell lymphoma outcome prediction by gene-expression profiling and supervised machine learning.* Nature medicine, 2002. **8**(1): p. 68.

[64] Caruana, R. and A. Niculescu-Mizil. *An empirical comparison of supervised learning algorithms*. in *Proceedings of the 23rd international conference on Machine learning*. 2006. ACM.

[65] Chapelle, O., B. Scholkopf, and A. Zien, *Semi-supervised learning (chapelle, o. et al., eds.; 2006)[book reviews]*. IEEE Transactions on Neural Networks, 2009. **20**(3): p. 542-542.

[66] Zhu, X., *Semi-supervised learning literature survey.* Computer Science, University of Wisconsin-Madison, 2006. **2**(3): p. 4.

[67] Furey, T.S., et al., *Support vector machine classification and validation of cancer tissue samples using microarray expression data.* Bioinformatics, 2000. **16**(10): p. 906-914.

[68] Joachims, T. *Text categorization with support vector machines: Learning with many relevant features*. in *European conference on machine learning*. 1998. Springer.

[69] Le, Q.V. *Building high-level features using large scale unsupervised learning*. in *Acoustics, Speech and Signal Processing (ICASSP), 2013 IEEE International Conference on*. 2013. IEEE.

[70] Hastie, T., R. Tibshirani, and J. Friedman, *Unsupervised learning*, in *The elements of statistical learning*. 2009, Springer. p. 485-585.

[71] Vincent, P., et al., *Stacked denoising autoencoders: Learning useful representations in a deep network with a local denoising criterion.* Journal of machine learning research, 2010. **11**(Dec): p. 3371-3408.

[72] Vincent, P., et al. *Extracting and composing robust features with denoising autoencoders*. in *Proceedings of the 25th international conference on Machine learning*. 2008. ACM.

[73] Mnih, V., et al., *Human-level control through deep reinforcement learning.* Nature, 2015. **518**(7540): p. 529.

[74] Noor, A.M., et al., *A microfluidic chip for capturing, imaging and counting CD3+ T-lymphocytes and CD19+ B-lymphocytes from whole blood.* Sensors and Actuators B: Chemical, 2018. **276**: p. 107-113.

[75] Mohamed, H., et al., *Isolation of tumor cells using size and deformation.* Journal of Chromatography A, 2009. **1216**(47): p. 8289-8295.

[76] Preira, P., et al., *Passive circulating cell sorting by deformability using a microfluidic gradual filter.* Lab on a Chip, 2013. **13**(1): p. 161-170.

[77] Kim, J., et al., *A high-efficiency microfluidic device for size-selective trapping and sorting.* Lab on a Chip, 2014. **14**(14): p. 2480-2490.

[78] Guo, Q., et al., *Deformability based Cell Sorting using Microfluidic Ratchets Enabling Phenotypic Separation of Leukocytes Directly from Whole Blood.* Scientific Reports, 2017. **7**(1): p. 6627.

[79] Walter, N., et al., *Direct assessment of living cell mechanical responses during deformation inside microchannel restrictions.* Biointerphases, 2011. **6**(3): p. 117-125.

[80] Schmid-Schönbein, G., et al., *Passive mechanical properties of human leukocytes.* Biophysical Journal, 1981. **36**(1): p. 243-256.

[81] Ji, H.M., et al., *Silicon-based microfilters for whole blood cell separation.* Biomedical microdevices, 2008. **10**(2): p. 251-257.

[82] Moazzam, F., et al., *The leukocyte response to fluid stress.* Proceedings of the National Academy of Sciences, 1997. **94**(10): p. 5338-5343.

[83] Hendrickx, A. and X. Bossuyt, *Quantification of the leukocyte common antigen (CD45) in mature B-cell malignancies.* Cytometry, 2001. **46**(6): p. 336-339.

[84] Baumgarth, N. and M. Roederer, *A practical approach to multicolor flow cytometry for immunophenotyping.* Journal of immunological methods, 2000. **243**(1-2): p. 77-97.

[85] Buggenthin, F., et al., *An automatic method for robust and fast cell detection in bright field images from high-throughput microscopy.* BMC bioinformatics, 2013. **14**(1): p. 297.

[86] Faustino, G.M., et al. *Automatic embryonic stem cells detection and counting method in fluorescence microscopy images*. in *Biomedical Imaging: From Nano to Macro, 2009. ISBI'09. IEEE International Symposium on*. 2009. IEEE.

[87] Dalal, N. and B. Triggs. *Histograms of oriented gradients for human detection*. in *Computer Vision and Pattern Recognition, 2005. CVPR 2005. IEEE Computer Society Conference on*. 2005. IEEE.

[88] Suykens, J.A. and J. Vandewalle, *Least squares support vector machine classifiers.* Neural processing letters, 1999. **9**(3): p. 293-300.

[89] Otsu, N., *A threshold selection method from gray-level histograms.* IEEE transactions on systems, man, and cybernetics, 1979. **9**(1): p. 62-66.

[90] Kamentsky, L., et al., *Improved structure, function and compatibility for CellProfiler: modular high-throughput image analysis software.* Bioinformatics, 2011. **27**(8): p. 1179-1180.

[91] Wiesmann, V., et al., *Review of free software tools for image analysis of fluorescence cell micrographs.* Journal of microscopy, 2015. **257**(1): p. 39-53.

[92] Xie, W., J.A. Noble, and A. Zisserman, *Microscopy cell counting and detection with fully convolutional regression networks.* Computer methods in biomechanics and biomedical engineering: Imaging & Visualization, 2018. **6**(3): p. 283-292.

[93] Nitta, N., et al., *Intelligent image-activated cell sorting.* Cell, 2018. **175**(1): p. 266-276. e13.

[94] Ota, S., et al., *Ghost cytometry.* Science, 2018. **360**(6394): p. 1246-1251.

[95] Bojarski, M., et al., *End to end learning for self-driving cars.* arXiv preprint arXiv:1604.07316, 2016.

[96] Parkhi, O.M., A. Vedaldi, and A. Zisserman. *Deep face recognition*. in *The British Machine Vision Conference (BMVC), 2015 International Conference on*. 2015. Swansea, UK.

[97] Cruz-Roa, A.A., et al. *A deep learning architecture for image representation, visual interpretability and automated basal-cell carcinoma cancer detection*. in *International Conference on Medical Image Computing and Computer-Assisted Intervention*. 2013. Springer.

[98] Chen, C.L., et al., *Deep learning in label-free cell classification.* Scientific reports, 2016. **6**: p. 21471.

[99] Saltz, J., et al., *Spatial organization and molecular correlation of tumor-infiltrating lymphocytes using deep learning on pathology images.* Cell reports, 2018. **23**(1): p. 181.

[100] Deng, J., et al. *Imagenet: A large-scale hierarchical image database*. in *Computer Vision and Pattern Recognition, 2009. CVPR 2009. IEEE Conference on*. 2009. Ieee.

[101] Cybenko, G., *Approximation by superpositions of a sigmoidal function.* Mathematics of control, signals and systems, 1989. **2**(4): p. 303-314.

[102] Pan, S.J. and Q. Yang, *A survey on transfer learning.* IEEE Transactions on knowledge and data engineering, 2010. **22**(10): p. 1345-1359.

[103] Krizhevsky, A., I. Sutskever, and G.E. Hinton. *Imagenet classification with deep convolutional neural networks*. in *Advances in Neural Information Processing Systems (NIPS), 2012 International Conferance on*. 2012. Lake Tahoe, Nevada, US.

[104] Simonyan, K. and A. Zisserman, *Very deep convolutional networks for large-scale image recognition.* arXiv preprint arXiv:1409.1556, 2014.

[105] Szegedy, C., et al. *Going deeper with convolutions*. in *Proceedings of the IEEE conference on computer vision and pattern recognition*. 2015.

[106] HIV/AIDS, J.U.N.P.o., *Global AIDS update 2016.* Geneva: UNAIDS, 2016.

Accomplishments

I. Journal Articles

[1] Turan, B., T. Masuda, A. M. Noor, K. Horio, T. I. Saito, Y. Miyata and F. Arai, *High accuracy detection for T-cells and B-cells using deep convolutional neural networks.* ROBOMECH Journal, 2018. **5**(1): p. 29.

[2] Turan, B., T. Masuda, W. Lei, A. M. Noor, K. Horio, T. I. Saito, Y. Miyata and F. Arai, *A pillar-based microfluidic chip for T-cells and B-cells isolation and detection with machine learning algorithm.* ROBOMECH Journal, 2018. **5**(1): p. 27.

II. International Conference Papers

[1] Turan, B., T. Masuda, W. Lei, A. M. Noor, K. Horio, T. I. Saito, Y. Miyata and F. Arai. *A Pillar-Based Microfluidic Chip for Detection of T-cells and B-cells using Machine Learning*. in *Micro-NanoMechatronics and Human Science (MHS), 2018 International Symposium on*. 2018. IEEE.

[2] Turan, B. and F. Arai. *Modeling the dead-band in magnetic actuation*. in *Micro-NanoMechatronics and Human Science (MHS), 2017 International Symposium on*. 2017. IEEE.

[3] Feng, L., B. Turan, U. Ningga and F. Arai. *Three dimensional rotation of bovine oocyte by using magnetically driven on-chip robot*. in *Intelligent Robots and Systems (IROS), 2014 IEEE/RSJ International Conference on*. 2014. IEEE.

[4] Sakuma, S., B. Turan, and F. Arai. *High throughput mechanical characterization of oocyte using robot integrated microfluidic chip*. in *Intelligent Robots and Systems (IROS), 2013 IEEE/RSJ International Conference on*. 2013. IEEE.

[5] Kakio, T., T. Bilal, S. Sakuma, M. Kaneko and F. Arai. *On-chip cellular force measurement by Direct-Outer-Drive mechanism*. in *Micro-NanoMechatronics and Human Science (MHS), 2013 International Symposium on*. 2013. IEEE.